Design, Growth, Fabrication and Characterisation of AlInGaAs/InP Lasers

Mykhaylo Veniaminovych Lysevych

A thesis submitted for the degree of

Master of Philosophy

of

The Australian National University

March 2007

This thesis contains no material which has been accepted for the award of any other degree or diploma in any university. To the best of the author's knowledge and belief, it contains no material previously published or written by another person, except where due reference is made in the text.

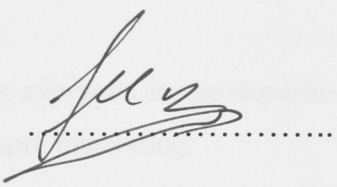

Mykhaylo Veniaminovych Lysevych

March, 2007

Acknowledgements

I would like to express my gratitude to those people, who have helped and supported me during my work on this project.

First, I would like to thank Prof. Chennupati Jagadish for his guidance, support and encouragement, and for always finding a spare minute to discuss my problems even if he was incredibly busy.

I would also like to thank Dr. Hoe Tan for his help with various techniques and equipment and for some very useful discussions. His knowledge of the MOCVD growth was immensely beneficial for the successful completion of this work.

My gratitude to Dr. Fu Lan for teaching me device processing and for her very helpful advices, as well as for always being very nice and friendly to me.

I also want to extend my gratitude to Dr. Manuela Buda for providing theoretical basis for this work and answering all my questions. Her knowledge of semiconductor lasers is extraordinary.

Many thanks to Dr. Michael Gao for his help with the SEM and Mr. Michael Aggett for the equipment maintenance.

Also I would like to thank everyone in the department of the EME for making my time at the department much more interesting.

I would like to acknowledge the Australian National University for financial support (in the form of the MPhil Scholarship).

Finally my biggest "THANK YOU" I want to address to my mother, and since she knows that I am a man of a few words, she will understand from it how much I appreciate her support.

And special thanks to Anna for putting up with me.

Abstract

This work addresses two major issues of the InP-based lasers: the thermal stability of the lasers and the output power at a single mode operation.

The use of AlInGaAs has been demonstrated to improve greatly the thermal stability of the InP-based lasers, but it is very challenging in terms of growth. The first part of this work deals with the optimisation of the MOCVD growth of AlInGaAs for InP-based lasers. The optimisation process was concentrated on the growth temperature, the V/III ratio and the growth rate. The optimised growth conditions allowed the growth of high quality material, with very narrow (55 nm) linewidth and high intensity room temperature photoluminescence of AlInGaAs layer. The results obtained during the optimisation process, were used later in this work for the growth of the laser structures.

The second part of this work concentrates on the issue of application of the thin p-clad design to InP-based lasers with InGaAs/AlInGaAs as the active region. The thin p-clad design is regarded to be an intermediate step towards a more novel asymmetric design, which would lead to the development of high power, single mode InP-based lasers. The thin p-clad lasers were fabricated, characterised and compared to the standard thick p-clad lasers. The measured internal quantum efficiency of the thick p-clad lasers (95 %) was one of the highest ever reported for the AlInGaAs/InP lasers. This value of the internal quantum efficiency once again proves good material quality of the laser structure. The comparison of both types of structures resulted in the increase of the internal losses for thin p-clad compared to the thick p-clad of only 4 cm^{-1}, which is in good agreement with theoretical model.

There is a great demand in the telecommunication industry for high power, single mode InP-based lasers since they can be used in transmitters as well as for pumping Raman amplifiers and erbium-doped fiber amplifiers. The results presented in this work can be used for the development of such lasers.

TABLE OF CONTENTS

Chapter 1

Introduction

1.1 Thesis Structure

This chapter introduces the reader to the motivation for the use of the thin p-clad laser structures, its advantages and disadvantages. The reasons for utilisation of AlInGaAs material as a barrier layer will be also briefly discussed here. Finally, the overview of the current status of the high power InP-based laser technology will be presented.

In Chapter 2 the experimental techniques and equipment used in this work will be presented. Chapter 3 deals with the issue of the material growth and its optimisation. The mathematical model used to design the laser structures will be discussed in Chapter 4. The characteristics of the lasers will be presented and analysed in Chapter 5. The summary of the work will be presented, and the ways for future work will be outlined in Chapter 6.

1.2 Motivation

In the era of Information Age the information or knowledge becomes the biggest asset. The need for acquiring and sharing information in the quickest and most efficient way is the driving force for the unprecedented expansion of the telecommunication networks. For the same reason the scientific community is investing a great amount of work into research and development of optical fiber, multiplexers, detectors, lasers, etc.

Plenty of interest has been drawn to lasers with the reduced thickness of the p-doped cladding layer (thin p-clad lasers) in the last decade [1-9]. The main reason for such interest is the possibility of the simplified fabrication of the distributed feedback (DFB) lasers. Due to much thinner p-cladding there would be enough coupling between the electromagnetic field and the periodic structure etched on top of the device. This would eliminate a very complicated regrowth step, which is necessary for the standard fabrication of DFB lasers [1].

The second reason is related to MOCVD growth of quantum dot (QD) lasers. Usually quantum dots are grown at a temperature of about 100 ^{o}C lower than the cladding layers. High growth temperature of the overlaying cladding layers strongly affects the dots, after they are formed. It leads to intermixing (which blueshifts and reduces the photoluminescence intensity) and finally dissociation of the dots [7]. Growing a structure with a thin p-clad can minimise these effects by substantially reducing the growth time of the cladding layers.

The characteristic temperature of a laser can be improved by simply mounting it p-side down on a heatsink [12]. Obviously such a mounting of thinner p-clad devices would result in even lower thermal resistance, therefore greatly improving the thermal stability of the lasers.

Another advantage of the thin p-clad is the possibility to apply impurity free disordering (IFD) technique to those devices. As was shown in refs. [13, 14] there is a strong correlation between the amount of the IFD of the active region and its distance from the surface. This phenomenon limits the use of IFD with thick p-clad devices, as the amount of the IFD might not be sufficient or the increased temperature needed for the sufficient amount of the IFD could cause a degradation of the devices.

Although thin p-clad design has many advantages there is one major disadvantage, which is the significant increase of the internal losses. Due to thinner p-clad the intensity of the optical field in the highly doped p-contact region is higher than that for the thick p-clad lasers. To overcome this problem an asymmetric design with reduced optical field intensity in the p-doped cladding layer was first proposed in ref. [15].

The internal absorption factor of p-doped layers is more than twice that of n-doped layers [16] and therefore, it is very desirable to minimise the losses in the p-doped layers. One way of doing this, is to reduce the doping of the p-clad layers, but due to low mobility of holes the resistance of the device increases rapidly with the decrease of the doping concentration, which in turn leads to other disadvantages.

Another way to reduce the free carrier absorption is to restrict or minimise the optical field penetration into the p-doped layers. This can be done by the use of the asymmetric design, which introduces a "trapping" layer into the laser structure. The trapping layer is a thick layer with high refractive index, placed in the n-doped region. A large portion of the optical field is shifted into the trapping layer, thereby reducing its penetration into the p-cladding, and hence decreasing the losses. Another advantage of the asymmetric design is better coupling to optical fiber. Since the optical field is not confined to narrow active region, the laser beam has smaller divergence. In this work the thin p-clad symmetric design is investigated, which is regarded as an intermediate step towards the asymmetric structure.

Another area of scientific interest is the improvement of the thermal characteristics of the lasers used for telecommunication applications. Since the poor thermal stability, due to small conduction band offset, is an inherent problem for InGaAs/InGaAsP/InP lasers, researchers turned their attention to InGaAs/AlInGaAs/InP material system. A better thermal stability of InGaAs/AlInGaAs material system is expected, due to higher conduction band offset, ($\Delta E_c = 0.7\ \Delta E_g$) compared to InGaAs/InGaAsP ($\Delta E_c = 0.4\ \Delta E_g$). A higher conduction band offset would lead to better electron confinement therefore lower electron leakage.

However the use of AlInGaAs/InP material system poses a serious challenge to the growth of high quality AlInGaAs. The growth of InGaAsP/InP structures requires a relatively low temperature to avoid In segregation, due to the high mobility of In. On the

other hand, high temperature is essential for the growth of good quality Al containing materials. Due to strong chemical bonds of Al-O and Al-C, a substantially higher temperature is necessary to break these bonds. The use of the low growth temperature (the typical temperature used for growth of InGaAsP) would lead to O and C incorporation into the AlInGaAs layer. These impurities would act as nonradiative recombination centers, which decrease the internal quantum efficiency and degrading the overall performance of the devices. Hence to grow good quality AlInGaAs, a compromise regime is required and there are indeed some encouraging reports [17, 18] demonstrating a great potential for AlInGaAs/InP material system in InP-based devices.

1.3 Current Status of High Power InP-Based Laser Technology

There is a great demand within the telecommunication industry for high power single mode lasers, operating in the range of 1400-1600 nm, since their application in transmitters, erbium-doped fiber amplifiers and Raman amplifiers increases the distance between the regenerators and the bandwidth of the network and therefore reduces its cost.

Generally, a high output power of a laser is achieved by increasing the width of the waveguide ridge of the laser, typically to a value of 100-200 μm. The power increases linearly with the increase of the ridge width, but the laser starts to operate in the multimode regime. Output power as high as 4.6 W has been reported for a laser with 200 μm wide ridge [10]. However, the multimode operation of those lasers makes it impractical to use them in fiber-optic networks, since most fibers deployed in those networks are single mode fibers.

The narrow ridge lasers can be tailored to operate in single mode regime, but their single mode output power is limited to less than 500 mW [21].

The advantages of both broad and narrow ridge lasers are blended together in flared structure lasers. The structure of a flared laser consists of two regions, a short narrow (single mode) ridge region and a long flared amplifying region. The narrow region filters

out the high order modes, while the flared region amplifies the mode supported by the resonator. A number of papers have been published, reporting the utilisation of the flared structures [19, 20, 23, 25]. A single mode operation with output power ranging from 1.1 W [19] to 2.1 W (1.1 W coupled into a fiber) [23] has been reported. However, due to highly nonsymmetrical optical field, coupling the output light from flared structure lasers into a fiber is a very difficult task which requires fairly complicated optic [23, 25]. Another disadvantage of this type of structure is the complicated fabrication, since a standard narrow ridge region does not provide sufficient filtering of the higher order modes. Extra measures, like the formation of channels next to the narrow ridge section, proton implantation, or distributed electrodes [19, 25] have to be undertaken to guarantee single mode operation.

Some very interesting results have been reported for a dual-channel ridge waveguide structure [22], where a single mode operation for λ = 1400 nm laser with the optical output of 1 W was demonstrated. The single mode operation is ensured by the strong confinement of the narrow (3 – 5 μm) dual-channel ridge waveguide, but the formation of these structures requires the etching through the active region. Therefore the lasers with dual-channel ridge waveguide structures cannot benefit from the utilisation of the AlInGaAs materials, since Al will oxidise if exposed to air.

The disadvantages and the benefits of the different designs currently used for high power lasers show the nonexistence of a clear leader in this area. This allows the lasers with the asymmetric design to occupy its individual niche in this rapidly expanding area.

References

[1] **"Low Loss, Thin p-clad 980-nm InGaAs Semiconductor Laser Diodes With an Asymmetric Structure Design"**, *M. Buda, J. Hay, H.H. Tan, J. Wong-Leung, and C. Jagadish, IEEE Journal of Quantum Electronics 39 (2003), 625-633.*

[2] **"Characterization of Thin p-Clad InGaAs Single-Quantum-Well Lasers"**, *C.H. Wu, P.S. Zory, and M.A. Emanuel, IEEE Photonics Technology Letters 7 (1995), 718-720.*

[3] **"Improvement of the Kink-Free Operation in Ridge-Waveguide Laser Diodes Due to Coupling of the Optical Field to the Metal Layers Outside the Ridge"**, *M. Buda, H.H. Tan, L. Fu, L. Josyula, and C. Jagadish, IEEE Photonics Technology Letters 15 (2003), 1686-1688.*

[4] **"Antiguided Array Diode Laser Fabricated with Modulated Cap Thin P-Clad Structure"**, *J. S. O, P. S. Zory, B. D. Schwartz, R. S. Setzko, M. A. Emanuel, and V. R. Sperry, IEEE Photonics Technology Letters 11 (1999), 415-417.*

[5] **"Abnormal Lasing Behaviors in Thin p-clad InGaAs Quantum Well Lasers"**, *C.H. Wu, P.S. Zory, and M.A. Emanuel, Solid-State Electronics 42 (1998), 405-410.*

[6] **"Contact Reflectivity Effects on Thin p-Clad InGaAs Single Quantum-Well Lasers"**, *C.H. Wu, P.S. Zory, and M.A. Emanuel, IEEE Photonics Technology Letters 6 (1994), 1427-1429.*

[7] **"Characteristics of MOCVD-Grown Thin p-Clad InGaAs Quantum-Dot Lasers"**, *P. Lever, M. Buda, H.H. Tan and C. Jagadish, IEEE Photonics Technology Letters 16 (2004), 2589-2591.*

[8] **"High Power CW Output from Low Confinement Asymmetric Structure Diode Laser"**, *G. Iordache, M. Buda, G.A. Acket, T.G. van de Roer, L.M.F. Kaufmann, F. Karouta, C. Jagadish and H.H. Tan, Electronics Letters 35 (1999), 148-149.*

[9] **"Low-Loss Low-Confinement GaAs-AlGaAs DQW Laser Diode with Optical Trap Layer for High-Power Operation"**, *M. Buda, W.C. van der Vleuten, Gh.*

Iordache, G.A. Acket, T.G. van de Roer, C.M. van Es, B.H. van Roy, and E. Smalbrugge, IEEE Photonics Technology Letters 11 (1999), 161-163.

[10] **"1.5 μm Wavelength, SCH-MQW InGaAsP/InP Broadened-Waveguide Laser Diodes with Low Internal Loss and High Output Power",** *D. Garbuzov, L. Xu, S.R. Forrest, R. Menna, R. Martinelli and J.C. Connolly, Electronics Letters 32 (1996), 1717-1719.*

[11] **"Monolithic Integration of an InGaAsP-InP MQW Laser/Waveguide Using a Twin-Guide Structure with a Mode Selection Layer",** *L. Xu, M.R. Gokhale, P. Studenkov, J.C. Dries, C.-P. Chao, D. Garbuzov, and S.R. Forrest, IEEE Photonics Technology Letters 9 (1997), 569-571.*

[12] **"Thermal Properties of 1.3 μm AlGaInAs Multi Quantum Well Ridge Waveguide Lasers",** *M. Kubota, K. Hamano, K. Takemasa, M. Kobayashi, H. Wada, T. Munakata, Japanese Journal of Applied Physics 39 (2000), 2297-2300.*

[13] **"Interdiffusion in InGaAs/GaAs Quantum Well Structures as a Function of Depth",** *W.P. Gillin, D.J. Dunstan, K.P. Homewood, L.K. Howard and B.J. Sealy, Journal of Applied Physics 73 (1993), 3782-3786.*

[14] **"Room-Temperature Exciton Transitions in Partially Intermixed GaAs/AlGaAs Superlattices",** *J.D. Ralston, S. O'Brien, G.W. Wicks and L.F. Eastman, Applied Physics Letters 52 (1988), 1511-1513.*

[15] **"Design of a 1W, Single Filament Laser Diode",** *I.B. Petrescu-Prahova, M. Buda and T.G. van der Roer, IEICE Trans. on Electr. E77-C (1994), 1472-1478.*

[16] **"Handbook of Semiconductor Lasers and Photonic Integrated Circuits",** – *edited by Y. Suematsu and A.R. Adams, Chapman & Hall, London, UK (1994).*

[17] **"Low-Threshold and High-Temperature Operation of InGaAlAs-InP Lasers",** *T.R. Chen, P.C. Chen, J. Ungar, M.A. Newkirk, S. Oh, and N. Bar-Chain, IEEE Photonics Technology Letters 9 (1997), 17-18.*

[18] **"High-performance phosphorus-free 1.3 μm AlGaInAs/InP MQW lasers",** *Jen-Wei Pan, Ming-Hong Chen, Jen-Inn Chyi, Journal of Crystal Growth 201/202 (1999), 923-926.*

[19] **"1.1-W Continuous-Wave 1480-nm Semiconductor Lasers with Distributed Electrodes for Mode Shaping",** *P. Salet, F. Gerard, T. Fillion, A. Pinquier, J.-L.*

Gentner, S. Delepine, and P. Doussiere, IEEE Photonics Technology Letters 10 (1998), 1706-1708.

[20] **"Tapered Laser Arrays for High Power Operation (>1.4W CW) at 1.59 μm for Application in Surgery",** *P.J. Williams, J.J. Lewandowski, D.J. Robbins, A.K. Wood, F.O. Robson, and B.K. Nayar, Electronics Letters 34 (1998), 993-994.*

[21] **"High Power InGaAsP/InP Broad-Waveguide Single-Mode Ridge-Waveguide Lasers",** *M. Maiorov, R. Menna, A. Komissarov, D. Garbuzov, and J. Connolly, Proceedings of the Optical Fiber Communication Conference and Exhibit 3 (2001), WC2-1 – WC2-3.*

[22] **"1400-1480 nm Ridge-Waveguide Pump Laser with 1 Watt CW Output Power for EDFA and Raman Amplification",** *D. Garbuzov, R. Menna, A. Komissarov, M. Maiorov, V. Khalfin, A. Tsekoun, S. Todorov, and J. Connolly, Proceedings of the Optical Fiber Communication Conference and Exhibit 4 (2001), PD18-1 – PD18-3.*

[23] **"Record 1 Watt Fiber-Coupled-Power 1480 nm Diode Laser Pump for Raman and Erbium Doped Fiber Amplification",** *A. Mathur, M. Ziari, V. Dominic, Proceedings of the Optical Fiber Communication Conference 4 (2000), 211 – 213.*

[24] **"High Power 1550 nm Distributed Feedback Lasers with 440 mW CW Output Power for Telecommunication Applications",** *R. Menna, A. Komissarov, M. Maiorov, V. Khalfin, L. DiMarco, J. Connolly, D. Garbuzov, Proceedings of the Lasers and Electro-Optics, CLEO. Technical Digest. Summaries of papers presented at the Conference on 6-11 May 2001 CPD12-1 – CPD12-2.*

[20] **"How to Launch 1 W into Single-Mode Fiber from a Single 1.48-μm Flared Resonator",** *S. Delepine, F. Gerard, A. Pinquier, T. Fillion, J. Pasquier, D. Locatelli, J.-P. Chardon, H.K. Bissessur, N. Bouche,F.R. Boubal, and P. Salet, IEEE Journal of Selected Topics in Quantum Electronics 7 (2001), 111-123.*

Chapter 2

Experimental Techniques

2.1 Introduction

In this chapter a short description of the experimental techniques used in this work will be provided. The purpose of this chapter is to present only the basic understanding of the techniques and the equipment used in this thesis. For more detailed description references have been provided at the end of the chapter.

The techniques discussed in this chapter relate to:

- Material growth (metalorganic chemical vapour deposition)
- Material characterisation techniques (photoluminescence, double crystal x-ray diffractometry, atomic force microscopy, electrochemical capacitance-voltage profiling)
- Device fabrication (photolithography, wet chemical etching, plasma enhanced chemical vapour deposition, rapid thermal processing, electron beam evaporation, cleaving)
- Device testing (light-current and spectral measurements)

2.2 Material Growth

2.2.1 Metalorganic Chemical Vapour Deposition

Metalorganic chemical vapour deposition (MOCVD) is an epitaxial technique widely used for growth of semiconductor materials. The principle behind this technique is the pyrolysis of compound source materials resulting in growth of the layer with the required material composition on a substrate.

All the structures used in this work were grown at the Australian National University by MOCVD. The MOCVD reactor used in this work is an AIXTRON AIX 200/4 horizontal flow reactor with wafer rotation. Rotation of the susceptor during the growth is aimed to improve uniformity of the growth. The deposition takes place at a reduced pressure of 180 mbar. The reactor is set up with: trimethylgallium (TMGa), trimethylindium (TMIn) and trimethylaluminium (TMAl) as the group III precursors, and arsine (AsH_3) and phosphine (PH_3) as the group V precursors. Arsine (AsH_3) and phosphine (PH_3) are gases, but trimethylgallium (TMGa) and trimethylaluminium (TMAl) are liquids and trimethylindium (TMIn) is solid at room temperature. Ultra high purity hydrogen is used as a carrier for the metalorganic precursors. Hydrogen is purified by passing it through palladium-silver alloy membrane. Diethylzinc (DEZn), carbon tetrachloride (CCl_4) are used as p- and silane (SiH_4) as n-type dopant precursors. Gas flow is precisely regulated by electronic mass flow controllers. Separate lines for group III and group V precursors are used, such that they do not mix and react until they get into the reactor. To minimise the transient effects during switching on/off of the gases, two set of lines are employed. One set called "Run" lines, another "Vent" lines. The "Run" lines go into the reactor, while the "Vent" lines bypass the reactor directly into the pump. The "Run/Vent" manifolds allow rapid switching between "Run" and "Vent" lines. A schematic of the MOCVD system is shown in Figure 2.1.

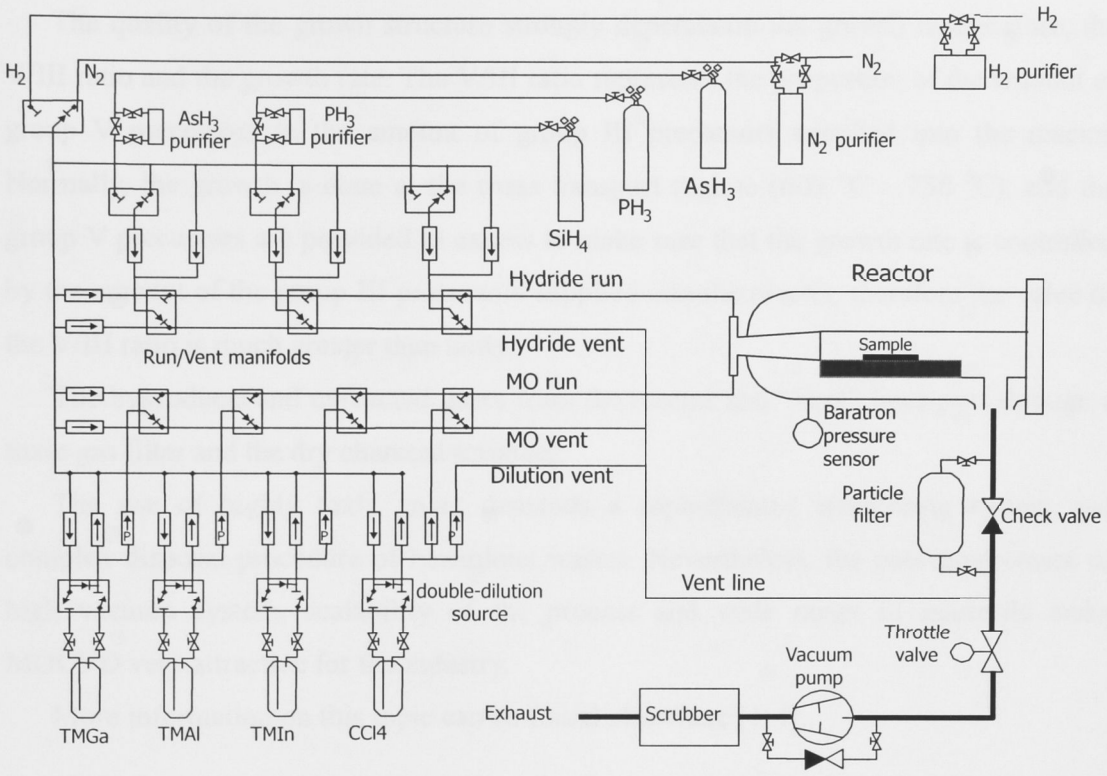

Figure 2.1 Schematic of the MOCVD (AIXTRON) system.

During growth the substrate is heated up to the growth temperature (600°C-750°C) by infra-red lamps. The high temperature causes pyrolysis of the precursors, the resultant radicals are chemically very active species, they diffuse towards the substrate, react and form a layer of the material on the substrate. This process also forms byproducts.

The general reactions, for common III-V compounds, that take place during the growth are:

$$In(CH_3)_3+PH_3 = \mathbf{InP}+3CH_4 \quad (2.1)$$

$$xIn(CH_3)_3+(1-x)Ga(CH_3)_3+AsH_3 = \mathbf{In_xGa_{(1-x)}As}+3CH_4 \quad (2.2)$$

$$xIn(CH_3)_3+(1-x)Ga(CH_3)_3+yAsH_3+(1-y)PH_3 = \mathbf{In_xGa_{(1-x)}As_yP_{(1-y)}}+3CH_4 \quad (2.3)$$

$$xAl(CH_3)_3+yIn(CH_3)_3+(1-x-y)Ga(CH_3)_3+AsH_3 = \mathbf{Al_xIn_yGa_{(1-x-y)}As}+3CH_4 \quad (2.4)$$

The quality of the grown structure strongly depends on the growth temperature, the V/III ratio and the growth rate. The V/III ratio represents the proportion of the amount of group V precursors to the amount of group III precursors supplied into the reactor. Normally, the growth is done at the mass transport regime (600 ^{o}C – 750 ^{o}C), and the group V precursors are provided in excess to make sure that the growth rate is controlled by the amount of the group III precursors supplied into the reactor, therefore the value of the V/III ratio is much greater than unity.

The byproducts and unreacted gases from the reactor and "Vent" lines pass through a toxic gas filter and the dry charcoal scrubber.

The use of highly toxic gases demands a sophisticated monitoring system and complex disposal procedure of hazardous wastes. Nevertheless, the non-requirement of high vacuum system, scalability of the process and wide range of materials make MOCVD very attractive for the industry.

More information on this topic can be found elsewhere [1-4].

2.3 Material Characterisation Techniques

2.3.1 Photoluminescence

Photoluminescence (PL) is a fundamental technique for characterisation of a semiconductor material. It is simple non-destructive technique employed to determine the bandgap of the material, as well as its quality.

The sample is illuminated with a monochromatic light with photons of energy higher than the bandgap of the sample. Photons are being absorbed by the material leading to the creation of electron-hole pairs. The electrons and holes then rapidly thermalise into the lowest possible states of the conduction band for electrons, and valence band for holes,

and recombine, generating photons with energy equal to the bandgap. The light is collected and measured after passing through a monochromator.

In this work the excitation was done using a frequency-doubled diode-pumped solid-state laser (λ=532 nm). To reduce noise, the laser light was chopped at around 300Hz and the photoluminescence signal was synchronised with the laser light through a lock-in amplifier. The photoluminescence was focused on the slit of a Digikrom 480 0.5m monochromator, and detected by a cooled InGaAs photodiode. A schematic of the photoluminescence set-up is shown in Figure 2.2.

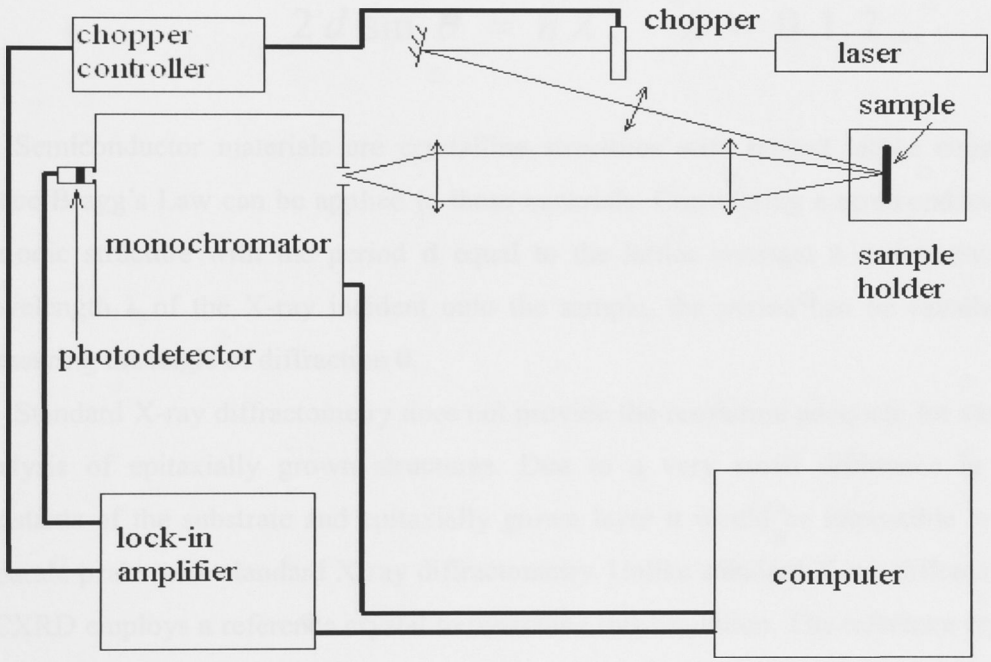

Figure 2.2 Schematic of the photoluminescence set-up.

Proper interpretation of the PL spectra is very important. The peak of the PL spectrum corresponds to the bandgap energy, while the full width at half maximum (FWHM) reflects the abruptness and the smoothness of the QW layer interfaces and also the degree of alloy fluctuation. The intensity of the PL is related to the quality of the layer.

More information on this topic can be found in ref. [5, 6].

2.3.2 Double Crystal X-Ray Diffractometry

Double crystal x-ray diffractometry (DCXRD) is a very important technique for epilayer analysis. DCXRD gives information about composition of the grown epilayer and its quality.

This technique is based on the Bragg diffraction. According to Bragg's Law, for electromagnetic wave with certain wavelength **λ** incident on a periodic structure with period d, there is a certain angle **θ** at which constructive interference will occur.

$$2d \sin \theta = n\lambda, \quad n = 0,1,2... \tag{2.5}$$

Semiconductor materials are crystalline structures with related lattice constant **a**, hence Bragg's Law can be applied to these materials. Considering a semiconductor as a periodic structure with the period **d** equal to the lattice constant **a** and knowing the wavelength **λ** of the X-ray incident onto the sample, the period can be calculated by measuring the angle of diffraction **θ**.

Standard X-ray diffractometry does not provide the resolution adequate for structural analysis of epitaxially grown structures. Due to a very small difference in lattice constants of the substrate and epitaxially grown layer it would be impossible to detect separate peaks with standard X-ray diffractometry. Unlike standard X-ray diffractometry, DCXRD employs a reference crystal to overcome this limitation. The reference crystal is employed to collimate the X-ray beam and to narrow its spectrum. Figure 2.3 illustrates the principle of a DCXRD system.

For quantitative analysis, DCXRD system employs equation derived from Bragg Law.

$$\frac{\Delta d}{d} = -\Delta\theta\cot\theta \tag{2.6}$$

Using this formula the distance difference between the crystallographic planes of the substrate and the epilayer (Δd) can be determined. But if the epilayer is under strain its

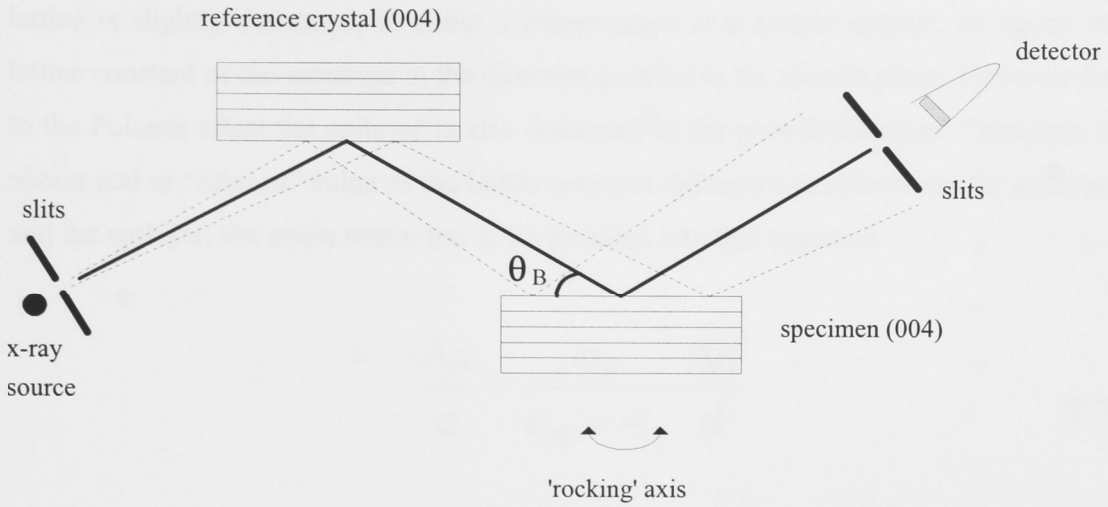

Figure 2.3 Schematic of a double-crystal X-ray diffractometer (DCXRD).

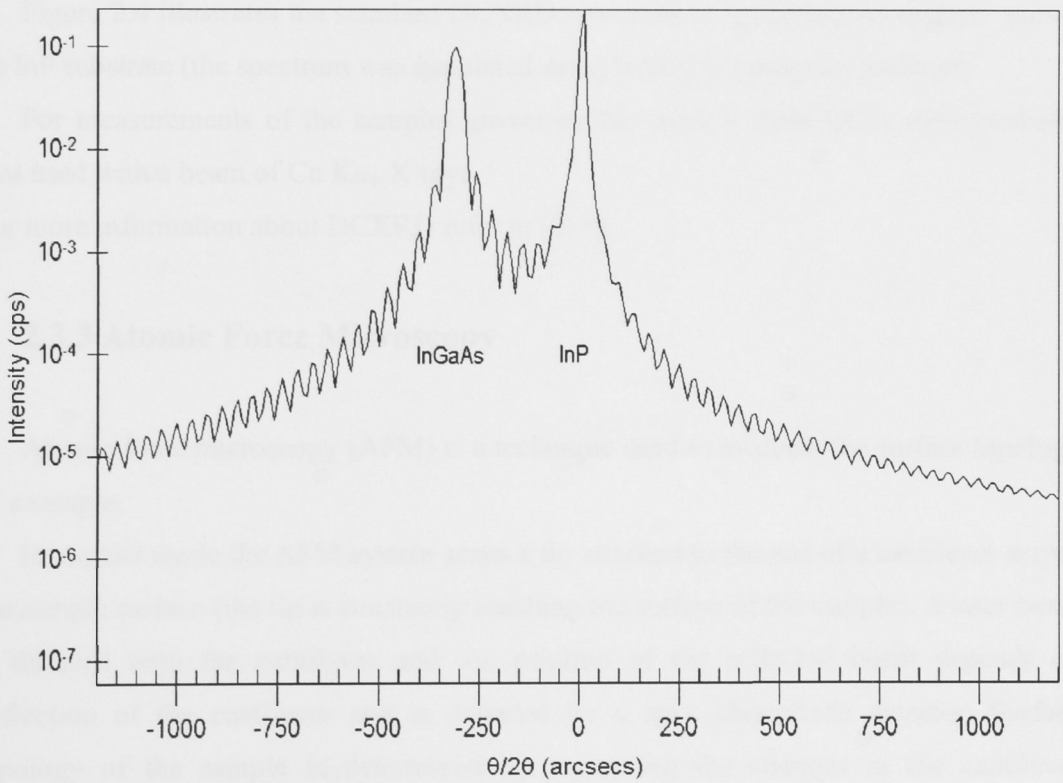

Figure 2.4 Simulated DCXRD spectrum of 5 μm $In_{0.54}Ga_{0.46}As$ grown on InP.

lattice is slightly deformed, in either a compressive or a tensile manner, to match the lattice constant of the substrate in the direction parallel to the growth plane. However due to the Poisson effect the epilayer is also deformed in the growth direction. Therefore, to obtain real or "relaxed" value of the lattice constant difference (Δa) between the substrate and the epilayer, the strain tensor has to be included into this equation:

$$\frac{\Delta a}{a} = \frac{\epsilon_{II}}{\epsilon_{II} - \epsilon_{\perp}} \frac{\Delta d}{d} \tag{2.7}$$

where $\epsilon_{\parallel}$ and $\epsilon_{\perp}$ are the strains of the lattice parallel and perpendicular to growth direction.

Figure 2.4 illustrates the standard DCXRD spectrum of $In_{0.54}Ga_{0.46}As$ epilayer grown on InP substrate (the spectrum was simulated using RADS [7] program package).

For measurements of the samples grown in this work a Bede QC2a diffractometer was used with a beam of Cu $K\alpha_1$ X-rays.

For more information about DCXRD refer to [8, 9].

2.3.3 Atomic Force Microscopy

Atomic force microscopy (AFM) is a technique used to evaluate the surface topology of a sample.

In contact mode the AFM system scans a tip attached to the end of a cantilever across the sample surface (the tip is constantly touching the surface of the sample). A laser beam is directed onto the cantilever and the position of the reflected beam depends on deflection of the cantilever and is detected by a split photodiode detector. Surface topology of the sample is determined by measuring the changes in the cantilever deflection. Figure 2.5 demonstrates the schematic of the AFM system running in contact mode.

The system used in this work is a Digital Instruments Nanoscope III Multimode AFM, with standard SiN tip. The system was operated in contact mode. A V-shape

cantilever with the SiN tip is attached to a piezoelectric scanner tube. The scanner tube can create movement along the three major axes. The backside of the cantilever is covered in gold to improve reflection of the laser beam. A feedback loop ensures a constant deflection of the cantilever.

In this work AFM was used to estimate the interfacial roughness of the sample's QWs by measuring the surface roughness.

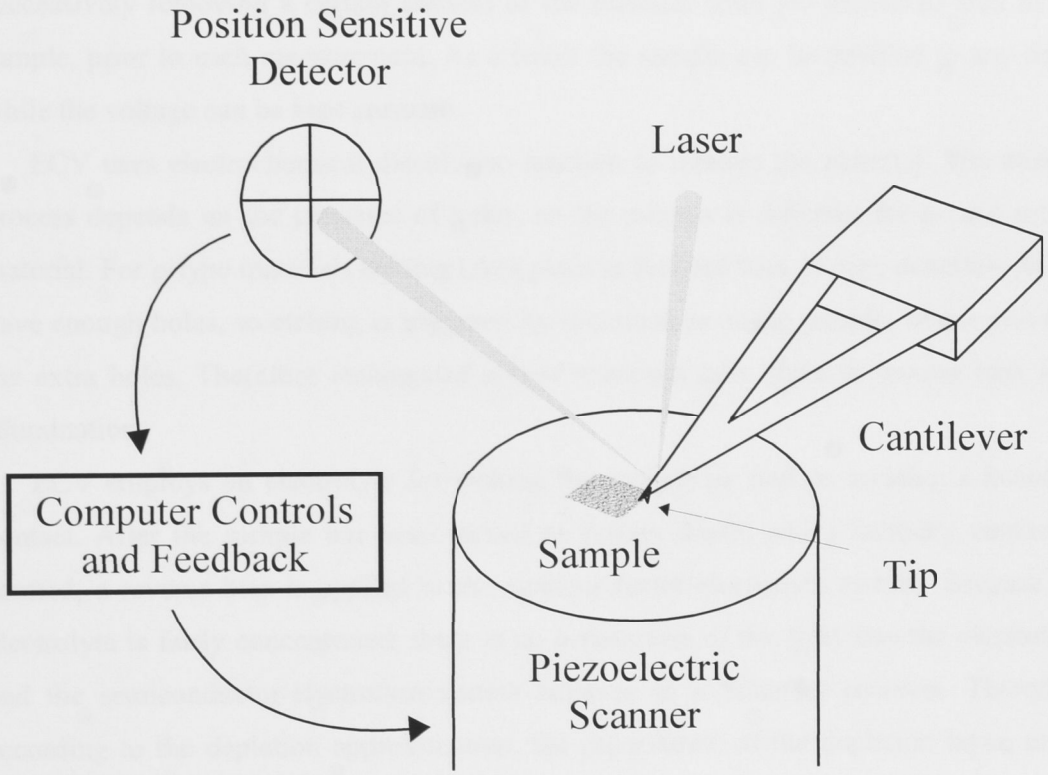

Figure 2.5 Schematic of the AFM system running in contact mode.

More information on this technique can be found in ref. [10, 11].

2.3.4 Electrochemical Capacitance-Voltage Profiling

The performance of all semiconductor devices depends on purity of the material and the precise distribution of carriers throughout the structure.

Electrochemical capacitance-voltage (ECV) profiling is a powerful technique for determining the doping profile in semiconductors [12, 13]. In standard CV measurements the impurity concentration is derived from the capacitance-voltage relationship of a reverse biased Schottky barrier. The main disadvantage of standard CV method is the depth of profiling, which is limited by the reverse breakdown voltage of the Schottky barrier. Electrochemical capacitance-voltage profiling overcomes this limitation by successively removing a certain amount of the material from the measured area of the sample, prior to each measurement. As a result the sample can be profiled to any depth while the voltage can be kept constant.

ECV uses electrochemical dissolution reaction to remove the material. The etching process depends on the presence of holes, so the process is different for p- and n-type material. For p-type materials etching takes place at forward bias. N-type materials do not have enough holes, so etching is triggered by illumination of the sample, which provides the extra holes. Therefore etchings of n-type materials take place at reverse bias with illumination.

ECV employs an electrolyte for etching the sample as well as creating a Schottky contact. After the sample has been etched to certain depth, and a Schottky contact is formed, a reverse bias is applied to the semiconductor-electrolyte system. Because the electrolyte is fairly concentrated, there is no penetration of the field into the electrolyte, and the semiconductor-electrolyte system behaves as a Schottky junction. Therefore, according to the depletion approximation, the capacitance of the depletion layer, under fixed reverse bias, can be described as:

$$C = \frac{\varepsilon A}{x} \tag{2.8}$$

where x is the depletion depth, C is the capacitance, A is the effective contact area, ε is the dielectric constant. The local doping density at certain x is given by:

$$N(x) = -\frac{C^3}{\varepsilon e A^2}\left(\frac{dC}{dV}\right)^{-1} \tag{2.9}$$

where A is the effective contact of etch area, C is the capacitance, ε is the dielectric constant, N(x) is the carrier concentration, e is the electron charge, V is the applied voltage, x is the depletion depth.

2.4 Device Fabrication

2.4.1 Summary of the Fabrication Process of Ridge-Waveguide Lasers

The following is the list of the fabrication steps arranged in order of the fabrication process of ridge-waveguide lasers.

1. Cleaning.
2. First photolithography (4 μm photoresist stripes).
3. Etching.
4. Si_3N_4 deposition.
5. "Lift-off" of Si_3N_4.
6. Annealing of Si_3N_4 (350°C 5min).
7. Second photolithography (50 μm photoresist stripes).
8. First p-side metallisation (Ti/Pt/Ti/Au – 10nm/20nm/40nm/50nm).
9. Polishing of the backside of the sample.
10. "Lift-off" of Ti/Pt/Ti/Au metal system.
11. N-side metallisation (Ge/Au – 20nm/200nm).
12. Alloying (450°C 30 s).
13. Final p-side metallisation (Au – 100nm).
14. Cleaving.

2.4.2 Photolithography

The laser processing requires two photolithography steps. The first step is to define the ridge, and the second is to cover the ridge before the Ti/Pt/Ti/Au deposition. The width of the mask stripes used is 4 μm and 50 μm for first and second photolithography steps respectively.

Prior to the first photolithography step, the samples were in turn cleaned using trichloroethylene, acetone, isopropanol and ethanol for two minutes each. To ensure no solvents were left on the sample surface, they were baked for 5 minutes at 85°C.

To improve photoresist adhesion to oxides, hexamethyldisilazane (HMDS) was applied to the samples surface before the second photolithography step.

Positive photoresist AZ5214E was spun on the samples at 4000 rpm for 30 seconds and "soft-baked" in an oven for 15 minutes at 85°C to harden the photoresist before the exposure.

A Karl Suss MA6/BA6 mask aligner was used to align the samples to the mask. The samples were aligned in $[0, 1, \bar{1}]$ crystallographic direction to form mesa shape ridges as shown in Figure 2.6 (b). After the alignment the samples were exposed to UV light for 25 seconds in the contact mode.

The samples were developed in 2:1 solution of the developer (AZ312) and water for 15 – 20 seconds. The quality of the stripes was checked using optical microscope. Finally the samples were "hard-baked" in an oven for 2 minutes at 120°C if subsequent etching has to be done.

For more information about photolithography refer to [14].

2.4.3 Wet Chemical Etching

Etching is one of the critical steps in laser fabrication process. Formation of the ridge is necessary for the lateral confinement of the electromagnetic field. The performance of the device strongly depends on the quality of the ridge and the etching depth.

The shape of the ridge is determined by the crystallographic direction in which the

stripes are aligned. Aligning the mask stripes in $[0, 1, \bar{1}]$ direction will produce a mesa shape ridge, while aligning the stripes in $[0, 1, 1]$ direction will produce a reverse mesa.

A practical way to find the right direction is to look for the direction of "etch pits" on the back side of the wafer. Because wafers are chemically polished, elongated ovals could be seen on the backside of the wafer under the microscope.

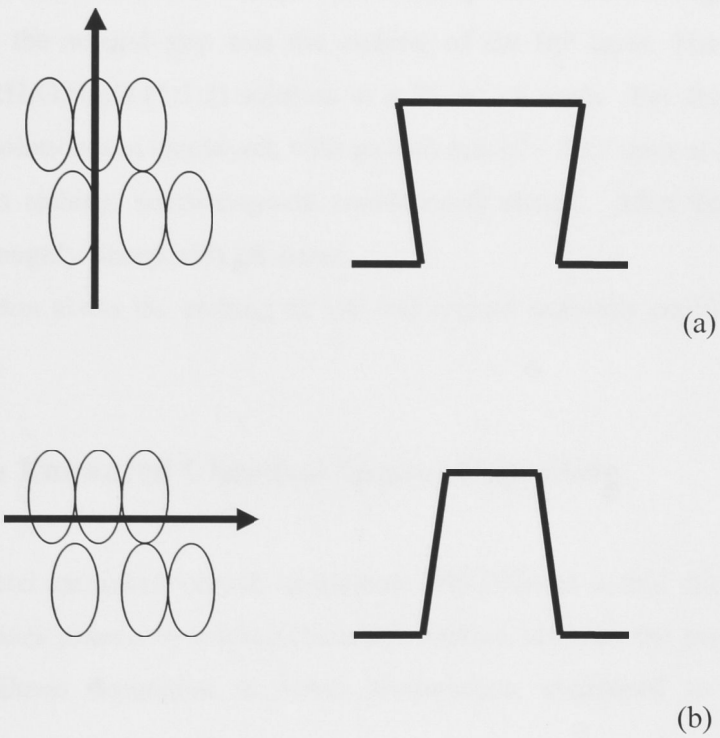

Figure 2.6 Dependency of the profile of the ridge on the direction of the stripes.

Aligning photoresist stripes parallel to the longer axis of these ovals will give a reverse mesa shape after the etching. A mesa shape ridge can be obtained by aligning photoresist stripes parallel to the shorter axis of these ovals. Figure 2.6 illustrates the dependency of the profile of the ridge on the direction of the stripes.

Choosing the right etchant for the formation of the ridge is very important. The criteria for a good etchant are: the etching should be fast, but controllable, the surface after the etching should be flat and uniform, with minimum undercutting and vertical sidewalls.

In this work two etching solutions were used. For InGaAs H_3PO_4:H_2O_2:H_2O (1:1:3) solution was used, while HCl:H_3PO_4 (1:3) was used for etching InP.

All the etching was done in a temperature controlled bath, at a constant temperature. The etching solutions were mixed for 30 minutes and then left in the temperature controlled bath for another 15 minutes, to stabilise the temperature.

The structures were etched in two steps. The first step was to etch through the InGaAs contact layer, and the second step was the etching of the InP layer. The etch rate of InGaAs in H_3PO_4:H_2O_2:H_2O (1:1:3) solution at 4 ^{o}C is ~ 8 nm/s. For the second step HCl:H_3PO_4 (1:3) solution was employed, with an etch rate of ~ 10.5 nm/s at 18 ^{o}C.

To get uniform etching, solutions were continuously stirred. After the etching the samples were thoroughly rinsed with DI water.

More information about the etching of InP and related materials could be found in references [15-27].

2.4.4 Plasma Enhanced Chemical Vapour Deposition

Plasma enhanced chemical vapour deposition (PECVD) is a thin film deposition technique that utilises plasma to initiate chemical reaction between the precursors. The use of plasma allows deposition at lower temperature, compared to other CVD techniques.

In this work PECVD was employed to deposit Si_3N_4. This is done to create an insulating layer, so current can be injected only through the top of the ridge.

All depositions were done using an Oxford Plasmalab 80 Plus PECVD system. It uses the principle of nonequilibrium glow discharge, generated by exposing the gas to a radio frequency (RF) electric field. The electric field accelerates free electrons in the gas. The electrons collide with the gas molecules, and if the electric field is high enough, the electrons can reach energies sufficient to ionise gas molecules. This process creates more free electrons, which in turn create more ionised gas, leading to avalanche ionisation and glow discharge. Some molecules undergo impact dissociation creating highly reactive species. These species diffuse towards the sample, adsorb on contact with the surface, undergo chemical reaction and surface migration, and eventually form a solid film.

Figure 2.7 shows a schematic of the PECVD system. Plasma is created between two parallel circular electrodes. The top electrode is connected to a 13.56 MHz RF generator, while the lower electrode is grounded. The samples are placed on the lower electrode. The reactant gases are fed in through the gas inlet in the top electrode.

For Si_3N_4 deposition 5 % silane (SiH_4) in nitrogen and ammonia (NH_3) were used. The deposition was made at 120 °C. The thickness of the deposited layer was 200 nm.

After the deposition, samples were soaked for few hours in acetone to remove photoresist together with Si_3N_4 from the top of the ridges, this procedure called "lift-off".

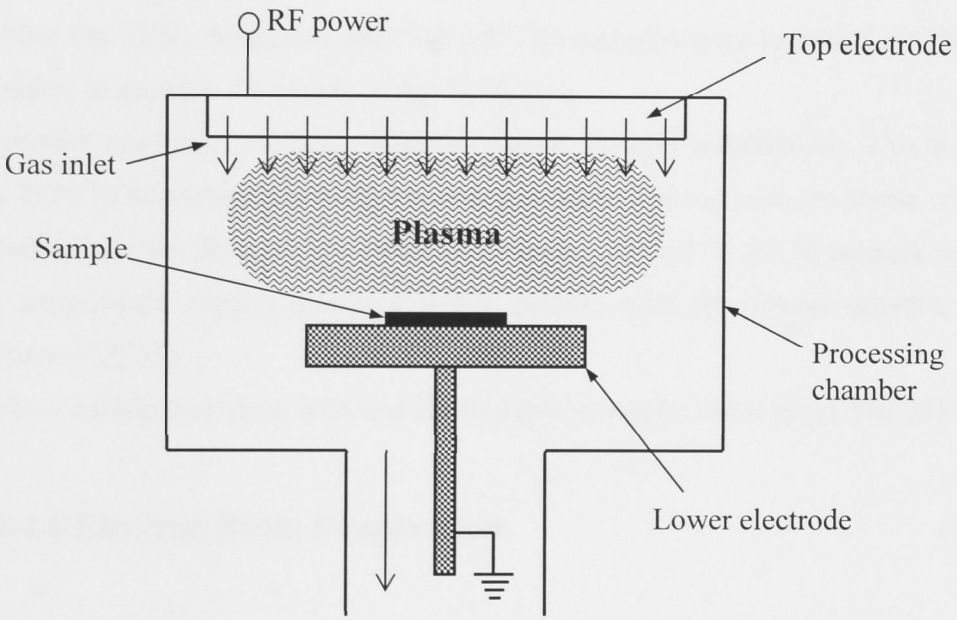

Figure 2.7 Schematic of the Oxford Plasmalab 80 Plus PECVD system.

For more information regarding PECVD refer to [28, 29].

2.4.5 Rapid Thermal Processing

Rapid thermal processing or rapid thermal annealing (RTA) was regularly employed throughout this work for different purposes. It relies on quartz-halogen lamps to heat the samples. A silicon wafer is used as the sample holder. Due to the small thermal mass of the heated wafer, temperature of the sample can be ramped up quickly. In order to create

an inert ambient, the chamber was filled with argon gas.

All the annealing was done with the use of AET Thermal Inc. RX rapid thermal annealer, in an Ar atmosphere. The temperature was ramped up at 100 °C/s till the required temperature was reached. The samples were annealed for the required amount of time, and then they were allowed to cool down in Ar ambient. Different time and temperature regimes were used for different processing steps. If the annealing temperatures were higher than 400 °C, the samples were protected using the proximity cap method (in which the samples were sandwiched between two pieces of InP wafer), to prevent loss of group V species.

After the Si_3N_4 deposition and "lift-off", the samples were annealed at 350 °C for 5 minutes, to improve the quality of the Si_3N_4 layer.

Another annealing was done after the second (n-side) metallisation. This is done to alloy Ti/Pt/Ti/Au system deposited between the ridges, and to create the ohmic contact on the backside of the devices. The temperature regime of 450 °C for 30 seconds was used. This temperature regime produces n-side contact with the lowest possible contact resistance [33, 34].

More information about RTA and ohmic contacts can be found in ref. [30-39]

2.4.6 Electron Beam Evaporation

Electron beam (e-beam) evaporation is another method of thin film deposition technique. It utilises a focused beam of electrons to heat and evaporate the source material. The evaporated material then deposits on all the surfaces of the chamber, including the samples. The deposition rate can be monitored by a quartz crystal. By changing the current of the electron beam the deposition rate can be adjusted. To improve the quality of the deposited layer deposition is performed in vacuum (~10^{-6} Torr).

A total of three e-beam evaporation steps were needed. First step was to deposit Ti/Pt/Ti/Au (10nm/20nm/40nm/50nm) on the p-side of the samples. The use of Ti/Pt system improves the adhesion between the contact layer and the sample's surface. After the first evaporation, samples were polished to about 100 μm, followed by the lift-off of the metal layer from the top of the ridges.

The second evaporation is to make the backside contact. During this step Ge/Au (20nm/200nm) were deposited on the n-side of the structure. High doping level of the sample is necessary for creation of good quality ohmic contact, therefore Ge is used to increase the doping of the InP substrate.

Finally a layer of Au (100nm) was deposited on the p-side of the samples. Annealing of the p-contact would create a very rough contact interface [34, 36, 38], which in the case of thin p-clad structure would introduce very high scattering losses. Therefore to keep the top of the ridge flat, no annealing was done after the final evaporation.

Native oxide layer was removed before Ge/Au and final Au evaporation. It was removed by dipping the samples into 3 % HCl solution for one minute.

2.4.7 Cleaving

The samples were cleaved into separate devices using a Loomis LSD-100 Scribe Dicing Machine. The samples were placed p-side up on the wafer holding film. Using notch and break mode the samples were cleaved into bars in the direction perpendicular to the laser ridges. Then using peck and break mode separate bars were diced into discrete devices. Lasers with cavity lengths ranging from 500 μm to 2 mm were made.

2.5 Device Testing

2.5.1 Light-Current Characterisation

The quality of the laser diodes can be assessed based on certain set of parameters. The majority of these parameters can be extracted from light-current (commonly referred to as L-I) measurements. Undoubtedly it is the most important characteristic of a semiconductor laser. The light power emitted by the laser is measured as a function of the injected current. Figure 2.8 demonstrates a typical light-current curve, the value of the

threshold current is denoted by I_{th}, where the lasing action commences.

To obtain an L-I curve the laser is placed p-side up onto the laser holder, which is connected to a laser diode driver. The laser holder is a copper block (cathode) with a copper clamp (anode). The temperature of the laser holder can be varied by the thermoelectric cooler placed in the copper block and regulated by a temperature controller.

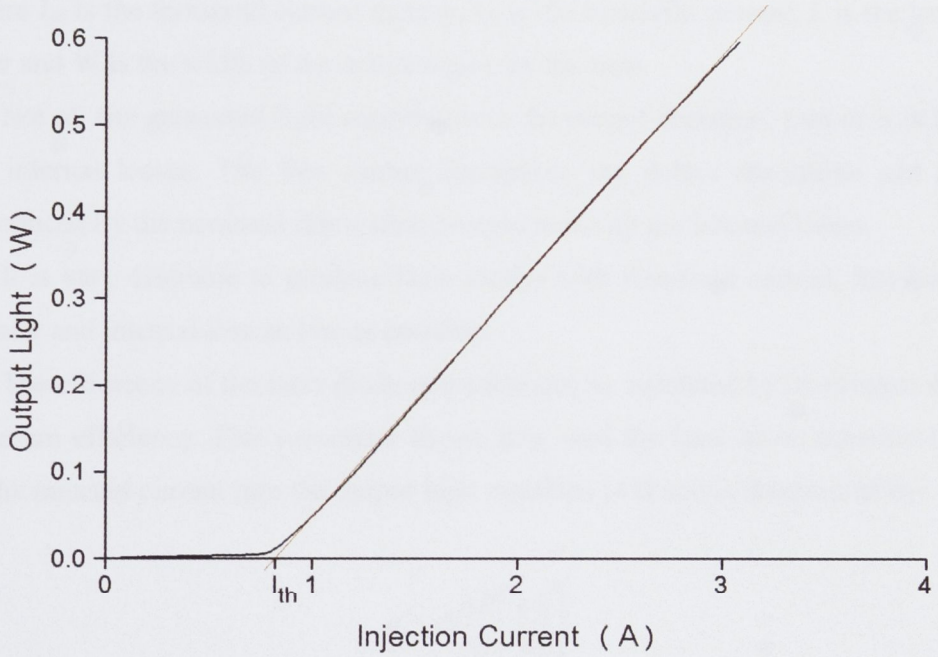

Figure 2.8 An example of a light-current curve. The threshold current is denoted by I_{th}.

Normally the lasers are mounted on a heatsink and run under continuous injection current. The use of a pulse current eliminates necessity of mounting lasers on a heatsink, which is a very time consuming process. The parameters of the pulse current are: 2 μs pulse width and a duty cycle of 5 %.

A variety of parameters can be extracted from L-I measurements and these include: threshold current, threshold current density, external differential quantum efficiency, internal quantum efficiency, internal loss and characteristic temperature.

The threshold current is the injection current at which the device starts to emit stimulated radiation, usually it is determined as the intercept point of the linear fit of the

L-I curve with the horizontal axis. Since the threshold current depends on the dimensions of the laser diode, it is more appropriate to use the threshold current density to compare the devices with different dimensions. The threshold current density is determined by:

$$J_{th} = \frac{I_{th}}{WL} \tag{2.10}$$

where J_{th} is the threshold current density, I_{th} is the threshold current, L is the length of the laser and W is the width of the active region of the laser.

Not all the generated light contributes to the output emission, part of it is lost due to the internal losses. The free carrier absorption, the defect absorption and the losses introduced by the nonideal fabrication process make up the internal losses.

It is very desirable to produce laser diodes with threshold current, threshold current density and internal loss as low as possible.

The efficiency of the laser diode operation can be estimated by its external differential quantum efficiency. This parameter shows how well the laser diode transfers the energy of the injected current into the output light emission [42] and is determined by:

$$\eta_d = 2\frac{\Delta P}{\Delta I}\left[\frac{q\lambda}{hc}\right] \tag{2.11}$$

where: η_d is the external differential quantum efficiency, $(\Delta P/\Delta I)$ is the slope of the L-I curve, q is the electron charge, h is Planck constant, c is the speed of light, and λ is the wavelength of the laser emission. It has to be mentioned that a laser diode emits light from both facets, but the light emitted from only one facet is measured, therefore the value of $(\Delta P/\Delta I)$ has to be doubled. Figure 2.9 illustrates an example of two L-I curves of lasers with different external differential quantum efficiency (the steeper is the curve the higher is the external differential quantum efficiency).

The internal quantum efficiency represents the fraction of injected electron-hole pairs that recombine radiatively [42]. Unlike the external differential quantum efficiency, it represents the quality of the laser structure. The external differential quantum efficiency

is related to the internal quantum efficiency through the relationship:

$$\frac{1}{\eta_d} = \frac{1}{\eta_i}\left[1 + \frac{\alpha_i}{\ln\left(\frac{1}{R}\right)}L\right] \tag{2.12}$$

where η_d is the external differential quantum efficiency, α_i is the internal loss, L is the laser cavity length, η_i is the internal quantum efficiency, and R is the reflectivity of the mirror-facet of the laser. Thus the internal quantum efficiency, as well as the internal loss can be determined by plotting the graph of the inverse external differential quantum efficiency as a function of the cavity length of the lasers. An example of such a graph is illustrated in Figure 2.10.

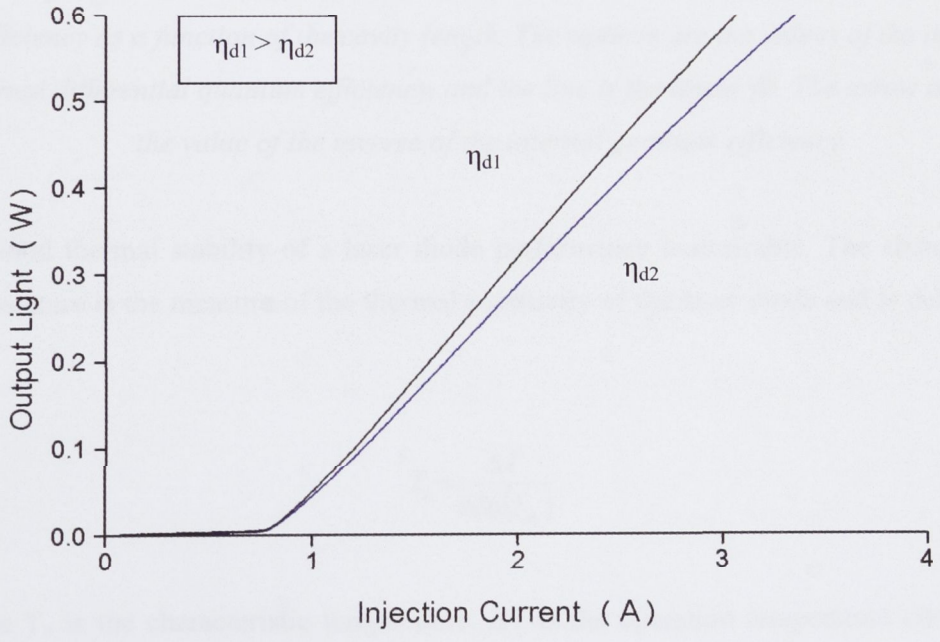

Figure 2.9 An example of the L-I curves of lasers with different external differential quantum efficiency.

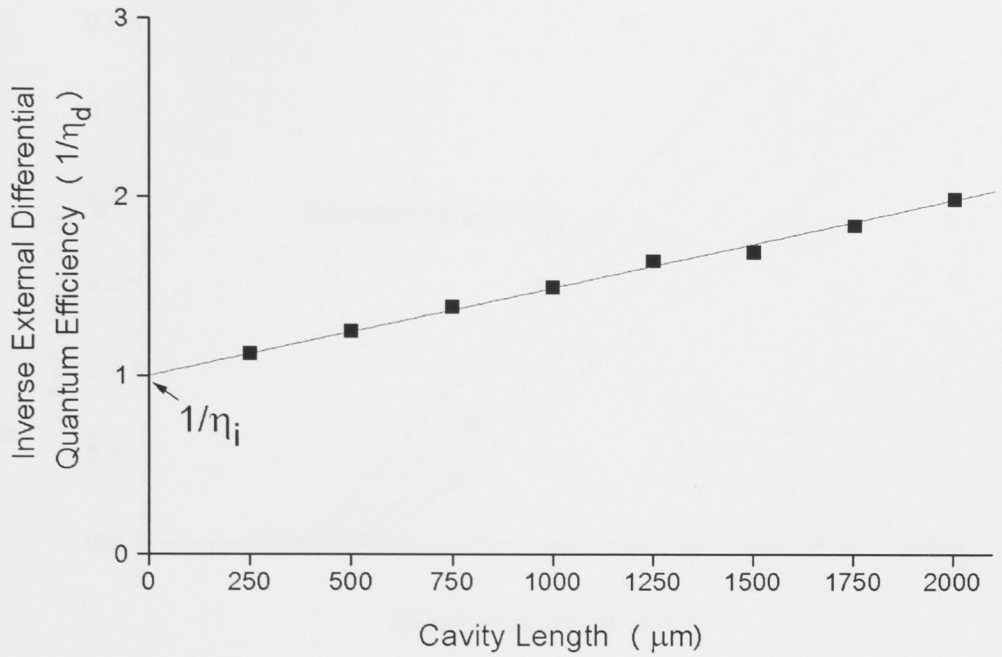

Figure 2.10 An example of the graph of the inverse external differential quantum efficiency as a function of the cavity length. The squares are the values of the inverse external differential quantum efficiency, and the line is the linear fit. The arrow indicates the value of the inverse of the internal quantum efficiency.

Good thermal stability of a laser diode performance is desirable. The characteristic temperature is the measure of the thermal sensitivity of the laser diode and is determined by:

$$T_o = \frac{\Delta T}{\Delta \ln(I_{th})} \tag{2.13}$$

where T_o is the characteristic temperature, ΔT is the operation temperature change and $\Delta \ln(I_{th})$ is the threshold current change on a logarithmic scale. A higher value of the characteristic temperature indicates that the laser diode parameters will change less rapidly with the change of operating temperature.

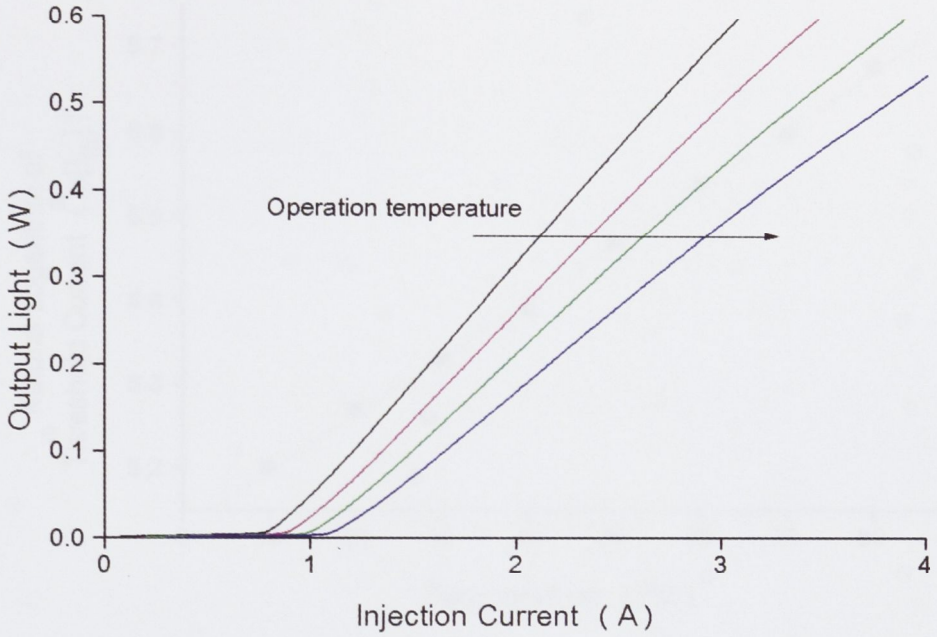

Figure 2.11 An example of the temperature dependent shift of an L-I curve.

To determine the characteristic temperature, series of L-I measurements are done at different operating temperatures. An example of temperature dependent shift of an L-I curve is shown in Figure 2.11. Then the value of the characteristic temperature is determined by plotting the graph of the threshold current against the operation temperature on a logarithmic scale and measuring the slope of the linear fit. The inverse of the slope of the linear fit is the value of the characteristic temperature. Figure 2.12 illustrates an example of the dependence of the threshold current as a function of operation temperature.

2.5.1 Spectral Measurements

The optical spectrum of a laser depends on the properties of the cavity and the bandgap of the material. Spectral measurements allow the determination of the modal

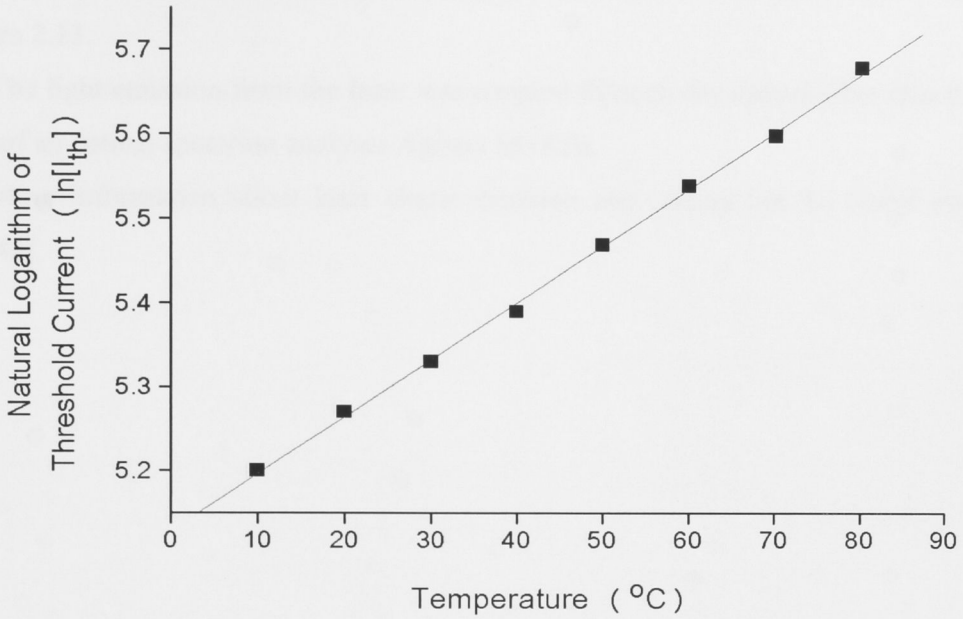

Figure 2.12 An example of the threshold current dependence as a function of operation temperature. The line is the linear fit.

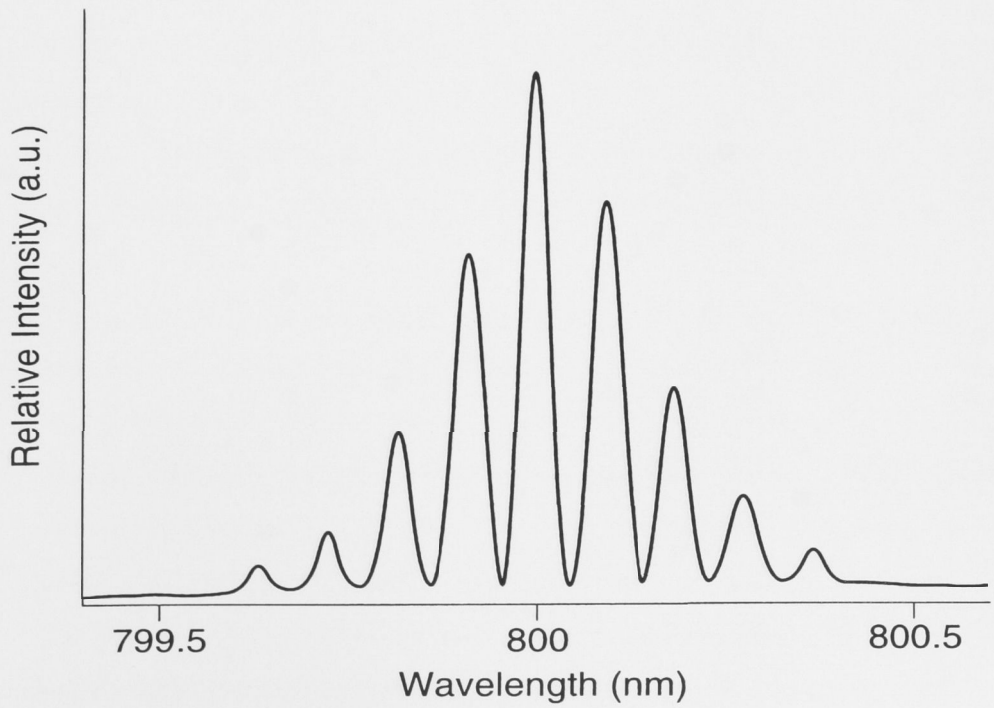

Figure 2.13 An example of the spectrum of a laser diode.

composition of the laser spectrum. A typical spectrum of a laser diode is shown in Figure 2.13.

The light emission from the laser was coupled through the optical fiber into the input port of an optical spectrum analyser Agilent 86142B.

More information about laser characterisation and testing can be found elsewhere [40-43].

References

[1] "**Metal-organic vapor phase epitaxy**", *T.F. Kuech, Material Science Reports 2 (1987), 1-50.*

[2] "**Organometallic vapor-phase epitaxy : Theory and practice**", *G.B. Stringfellow, Academic Press, San Diego (1989).*

[3] **"Metalorganic chemical vapor deposition", in III-V semiconductor materials and devices,** *J.J. Coleman and P.D. Dapkus, R. J. Malik, editor, North Holland Publishers, Amsterdam (1989).*

[4] **"Operation manual",** *Aixtron, www.aixtron.com.*

[5] **"Photoluminescence I : Theory",** *Chp. 4, 182-320 in Semiconductors and Semimetals, Vol. 8, Transport and Optical Phenomena, H.B. Bebb and E.W. Williams. R.K. Willardson and A.C. Beer, editors, Academic Press, New York (1972).*

[6] **"Optical processes in semiconductors",** *J.I. Pankove, Dover Publications Inc., New York (1971).*

[7] **"RADS (Rocking curve Analysis by Dynamical Simulation)",** *Bede Scientific Instruments Ltd. U.K., version 2.00 (1993)*

[8] **"High resolution x-ray diffraction and topography for crystal characterization",** *B.K. Tanner, Journal of Crystal Growth 99 (1990), 1315-1323.*

[9] **"Advanced X-ray scattering techniques for the characterization of semiconducting materials",** *B.K. Tanner and D.K. Bowen, Journal of Crystal Growth 126 (1993), 1-18.*

[10] **"Atomic force microscope",** *G. Binnig, C.F. Quate, and Ch. Gerber, Physical review letters 56 (1986), 930-933.*

[11] "**Nanoscope Training Manual",** *Nanoscope, 2002.*

[12] **"The electrical characterization of semiconductors : Majority carriers and electron states",** *P. Blood and J.W. Orton, Academic Press, London (1992).*

[13] **"PN4300PC electrochemical C-V profiler with photovoltage spectroscopy",** *Operating manual, Bio-Rad Micromeasurements, 1994.*

[14] **"Semiconductor lithography: Principles, practices and materials",** *W. M. Moreau, Plenum Press, New York, (1988).*

[15] **"Low-threshold 1.5 µm DFB laser grown by GSMBE",** *B. Fernier, C. Artigue, D. Bonnevie, L. Goldstein, A. Perales, J. Benoit, Electronics Letters 25 (1989), 768-770.*

[16] **"Grating formation by chemical etching in AlInAs for MQW devices",** *G. Meneghini, Electronics Letters 25 (1989), 725-726.*

[17] **"Local etch-rate control of masked InP/InGaAsP by diffusion-limited etching",** *T. Brenner, H. Melchior, Journal of the Electrochemical Society 141 (1994), 1954-1956.*

[18] **"InP in HBTs by vertical and lateral wet etching",** *N. Matine, M.W. Dvorak, J.L. Pelouard, F. Pardo, and C.R. Bolognesi, 1998 International Conference on Indium Phosphide and Related Materials (Cat. No.98CH36129). IEEE. 1998, pp.195-8. New York, NY, USA.*

[19] **"AlAs Etch-Stop Layers for InGaAlAs/InP Heterostructure Devices and Circuits",** *T.P.E. Broekaert and C.G. Fonstad, IEEE Transactions on Electron Devices 39 (1992), 533-536.*

[20] **"Wet chemical etching for V-grooves into InP Substrates",** *J. Wang, D.A. Thompson, and J.G. Simmons, Journal of the Electrochemical Society 145 (1998), 2931-2937.*

[21] **"SEM and AFM characterization of high-mesa patterned InP substrates prepared by wet etching",** *P. Elias, V. Chambel, S. Hasenohrl, P. Hudek, J. Novak, Materials Science and Engineering B 66 (1999), 15-20.*

[22] **"Fabrication of InP/GaInAs double heterojunction bipolar transistors with a 0.1-µm-wide emitter",** *T. Morita, T. Arai, H. Nagatsuka, Y. Miyamoto and K. Furuya, Japanese Journal of Applied Physics 41 (2002), L121-L123.*

[23] **"Etching of gain-coupled gratings into a multi-quantum-well laser with selective wet etches",** *R. Finlay, Journal of Vacuum Science & Technology A 22 (2004), 1054-1057.*

[24] **"Chemical etching of InP and GaInAsP for fabricating laser diodes and integrated optical circuits",** *T. Kambayash, C. Kitahara and K. Iga, Japanese Journal of Applied Physics 19 (1980), 79-85.*

[25] **"Etch rates for two material selective etches in the InGaAsP/InP system",** *K.L. Conway, A.G. Dentai, and J.C. Campbell, Journal of Applied Physics 53 (1982), 1836-1838.*

[26] **"Fabrication and characterization of 0.2 to 6 μm GaInAs/InP electron waveguides",** *I. Maximov, Q. Wang, M. Graczyk, P. Omling, L. Samuelson, W. Seifert, I. Shorubalko, K. Hieke, S. Lourdudoss, and E.R. Messmer, Proceedings of the Indium Phosphide and Related Material. Eleventh International Conference on 16-20 May 1999.*

[27] **"Fabrication and characterization of dry and wet etched InGaAs/InGaAsP/InP long wavelength semiconductor lasers",** *B. Cakmak, Optics Express 10 (2002), 530-535.*

[28] **"Handbook of plasma processing technology: Fundamentals, etching, deposition, and surface interactions",** *R. Reif, S. M. Rossnagel, J. J. Cuomo, and W. D. Westwood, Eds. Westwood: Noyes Publicaitons, 1990.*

[29] **"Glow discharge processes",** *B. Chapman, New York: John Wiley, 1980.*

[30] **"Rapid thermal processing",** *R. B. Fair, Academic Press, San Diego (1993).*

[31] **"Pt/Ti/p-$In_{0.53}Ga_{0.47}As$ low-resistance nonalloyed ohmic contact formed by rapid thermal processing",** *A. Katz, W.C. Dautremont-Smith, S.N.G. Chu, P.M. Thomas, L.A. Koszi, J.W. Lee, V.G. Riggs, R.L. Brown, S.G. Napholtz, and J.L. Zilko, Applied Physics Letters 54 (1989), 2306-2308.*

[32] **"Evaluation of single ohmic metallisations for contacting both p- and n-type GaInAs",** *L.G. Shantharama, H. Schumacher, H.P. Leblanc, R. Esagui, R. Bhat, M. Koza, Electronics Letters 26 (1990), 1127-1129.*

[33] **"AuGe/Au ohmic contacts to n-type InP by hot-plate alloying",** *S.C. Binari, J.B. Boos, Electronics Letters 25 (1989), 1207-1209.*

[34] **"The impact of the surface roughness on the electrical properties of AuGeNi/n-InP ohmic contacts",** *T. Clausen, O. Leistiko, Semiconductor Science and Technology 10 (1995), 691-697.*

[35] **"Low resistance 1.55 μm InGaAsP/InP semi-insulating buried heterostructures laser diodes using a multilayer contact structure",** *S. Matsumoto, R. Iga, Y. Kadota, M. Yamamoto, M. Fukuda, K. Kishi and Y. Itaya, Electronics Letters 31 (1995), 882-883.*

[36] **"Scanning transmission electron microscopy study of Au/Zn/Au/Cr/Au and Au/Ti/Au/Cr/Au contacts to p-type InGaAs/InP",** *J.S. Huang, C.B. Vartuli, Journal of Applied Physics 93 (2003), 5196-5200.*

[37] **"A survey of ohmic contacts to III-V compound semiconductors",** *A.G. Baca, F. Ren, J.C. Zolper, R.D. Briggs, S.J. Pearton, Thin Solid Films 308-309 (1997), 599-606.*

[38] **"Influence of the electrical contact on the reliability of InP-based ridge waveguide distributed feedback semiconductor diode laser for telecommunications applications",** *S. Zhang, M.G. Boudreau, R. Kuchibhatla, Y. Tao, S.R. Das, E.M. Griswold, and U. Sharma, Journal of Vacuum Science & Technology A 22 (2004), 803-806.*

[39] **"Pt/Ti ohmic contact to p^{++}-InGaAsP (1.3 μm) formed by rapid thermal processing",** *A. Katz, P.M. Thomas, S.N.G. Chu, W.C. Dautremont-Smith, R.G. Sobers, and S.G. Napholtz, Journal of Applied Physics 67 (1990), 884-889.*

[40] **"Semiconductor optoelectronics: Physics and technology",** *J. Singh, McGraw-Hill, Singapore (1995).*

[41] **"Semiconductor optoelectronic devices",** *P. Bhattacharya, Prentice-Hall, New Jersey (1997).*

[42] **"Semiconductor lasers",** *G. P. Agrawal, N. K. Dutta, Kluwer Academic Publisher, Massachusetts (2000).*

[43] **"Test and characterisation of laser diodes: Determination of principal parameters",** *K. S. Mobarhan, www.newport.com*

Chapter 3

Material Growth

3.1 Introduction

The cornerstone of a high-performance semiconductor laser is its material quality. As for QW lasers, the abruptness and flatness of interfaces of the QW layers are as crucial as the material quality. The growth parameters have to be optimised to obtain epitaxially grown structure with good material quality, minimum alloy fluctuation, abrupt and flat interfaces.

This chapter is devoted to the growth optimisation of the samples used in this work, in particular AlInGaAs materials. The issues of precise control of material composition and influence of growth parameters (like growth temperature, growth rate and V/III ratio) on the quality of grown material will be presented and discussed.

3.2 Material Composition and Growth Rate

Precise control of the material composition is essential for device applications such as laser diodes. There are two major reasons why material composition is so important. Firstly, the grown material has to satisfy the condition of lattice matching, to avoid dislocations which would ruin the devices. Secondly, the operational wavelength of the laser diode depends on the bandgap of the QW layer, which is also dependent on the material composition.

All the structures were grown on (001) InP on-axis (± 0.05°) substrates by MOCVD. The sources used were trimethylgallium (TMGa), trimethylindium (TMIn), trimethylaluminium (TMAl) and arsine (AsH_3) and phosphine (PH_3). The reactor pressure was kept at 180 Torr.

For ternary and quaternary materials, the fractions of elements of the same group (group III or group V) in solid material do not follow exactly fractions of the respective precursors in the vapour phase. Usually calibration runs have to be done to determine these relations. Figures 3.1, 3.2, 3.3 and 3.4 represent the empirically determined calibration curves for various elements of different materials.

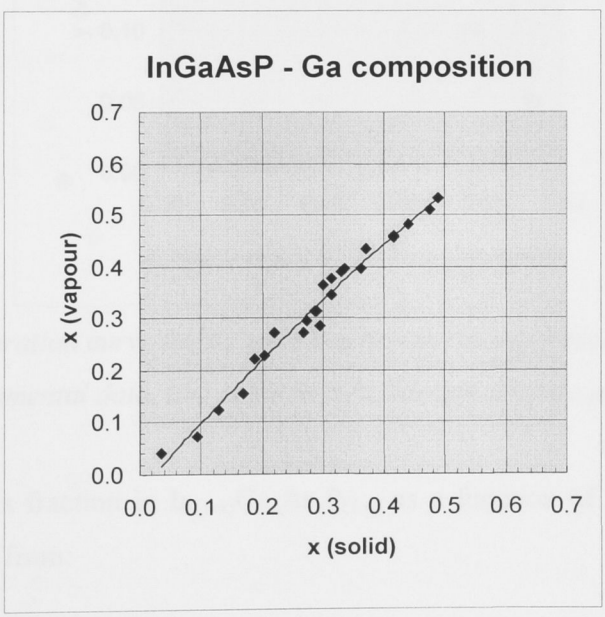

Figure 3.1 Calibration curve for Ga mole fraction in InGaAsP (solid points are the experimental data, line is the best fit through all data points).

The material composition of the $In_{(1-x)}Ga_xAs_yP_{(1-y)}$ can be determined from equations deduced from the respective calibration curves. The Ga fraction in $In_{(1-x)}Ga_xAs_yP_{(1-y)}$ as a function of TMIn and TMGa flow rates can be defined from:

$$x(v) = -0.3272x^2(s) + 1.3143x(s) - 0.0299 \tag{3.1}$$

$$x(v) = \frac{F(TMGa)}{F(TMGa) + F(TMIn)} \tag{3.2}$$

where: x(s) is the Ga fraction in the solid material, x(v) is the fraction of TMGa in the vapour phase, F(TMGa) and F(TMIn) are the flow rates of TMGa and TMIn respectively.

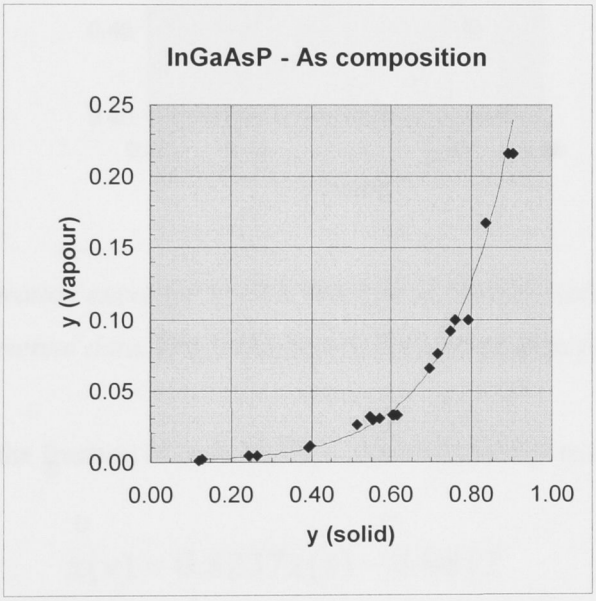

Figure 3.2 Calibration curve for As mole fraction in InGaAsP (solid points are the experimental data, line is the best fit through all data points).

Similarly the As fraction in $In_{(1-x)}Ga_xAs_yP_{(1-y)}$ as a function of AsH_3 and PH_3 flow rates can be defined from:

$$y(v) = (8.207 \cdot 10^{-4})e^{6.287 \cdot y(s)} \tag{3.3}$$

$$y(v) = \frac{F(AsH_3)}{F(AsH_3) + F(PH_3)} \tag{3.4}$$

where: y(s) is the As fraction in the solid material, y(v) is the fraction of AsH_3 in the vapour phase, $F(AsH_3)$ and $F(PH_3)$ are the flow rates of AsH_3 and PH_3 respectively.

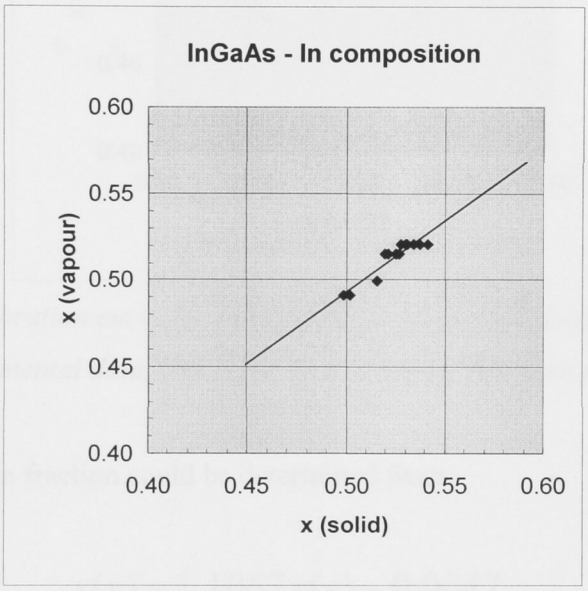

Figure 3.3 Calibration curve for In mole fraction in InGaAs (solid points are the experimental data, line is the best fit through all data points).

In the same way the fraction of In in $In_xGa_{(1-x)}As$ could be determined from:

$$x(v) = 0.8237x(s) - 0.0812 \tag{3.5}$$

$$x(v) = \frac{F(TMIn)}{F(TMGa) + F(TMIn)} \tag{3.6}$$

where: x(s) is the In fraction in the solid material, x(v) is the fraction of TMIn in the vapour phase, F(TMGa) and F(TMIn) are the flow rates of TMGa and TMIn respectively.

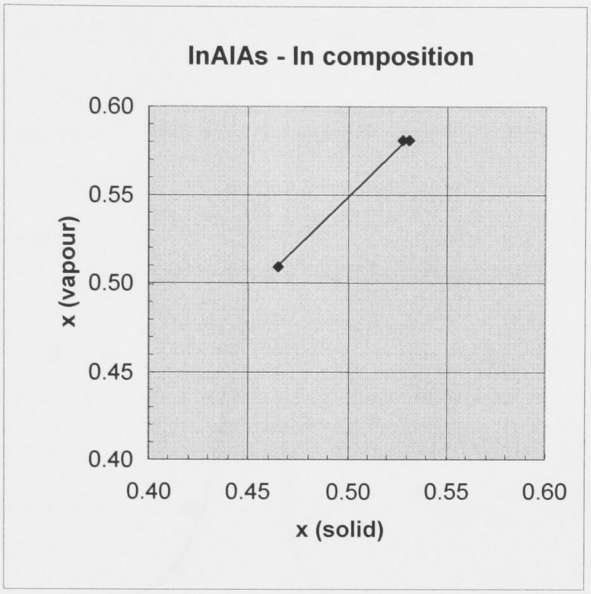

Figure 3.4 Calibration curve for In mole fraction in InAlAs (solid points are the experimental data, line is the best fit through all data points).

For $In_xAl_{(1-x)}As$ In fraction could be determined from:

$$x(v) = 1.1067x(s) - 0.0047 \tag{3.7}$$

$$x(v) = \frac{F(TMIn)}{F(TMIn) + F(TMAl)} \tag{3.8}$$

where: x(s) is the In fraction in the solid material, x(v) is the fraction of TMIn in the vapour phase, F(TMAl) and F(TMIn) are the flow rates of TMAl and TMIn respectively.

All the data points in the Figure 3.3 and Figure 3.4 are located in the vicinity of x(s) = 0.53 for InGaAs and 0.52 for InAlAs which are the lattice matching conditions for those materials grown on InP substrate. Within this small region, the data can be approximated with good accuracy with straight lines.

In the case of $Al_{x'}In_{x''}Ga_{(1-x'-x'')}As$ three variables (In, Al, Ga), or two independent variables exist, therefore calibration curves of InAlAs and InGaAs were taken as a starting point. Because GaAs and AlAs are lattice matched materials, replacing Al in InAlAs (lattice matched to InP) with Ga will also result in lattice matching condition for

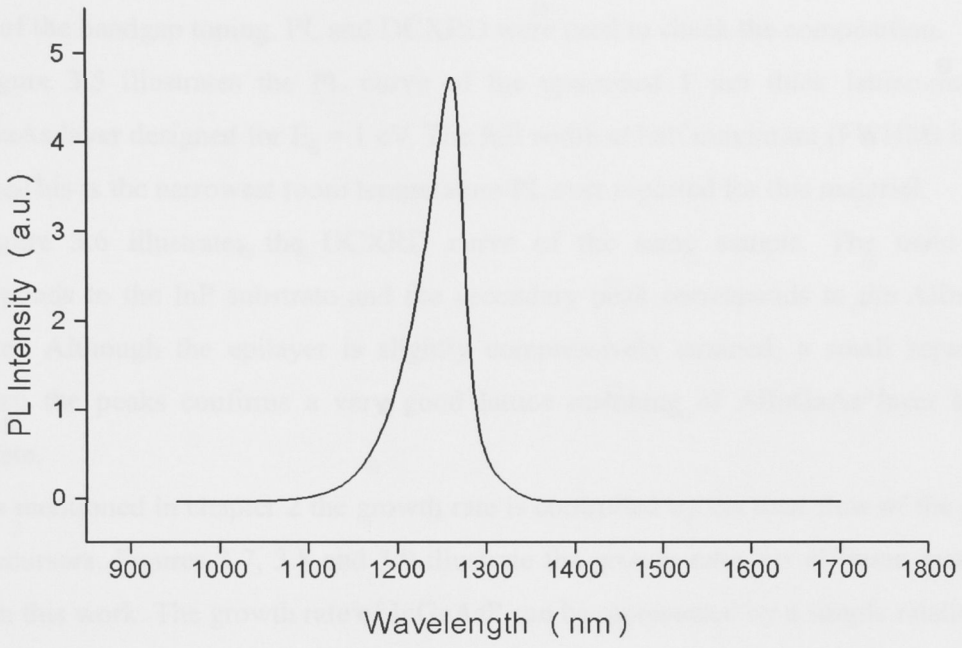

Figure 3.5 PL curve of a 1 μm thick AlInGaAs layer grown on InP.

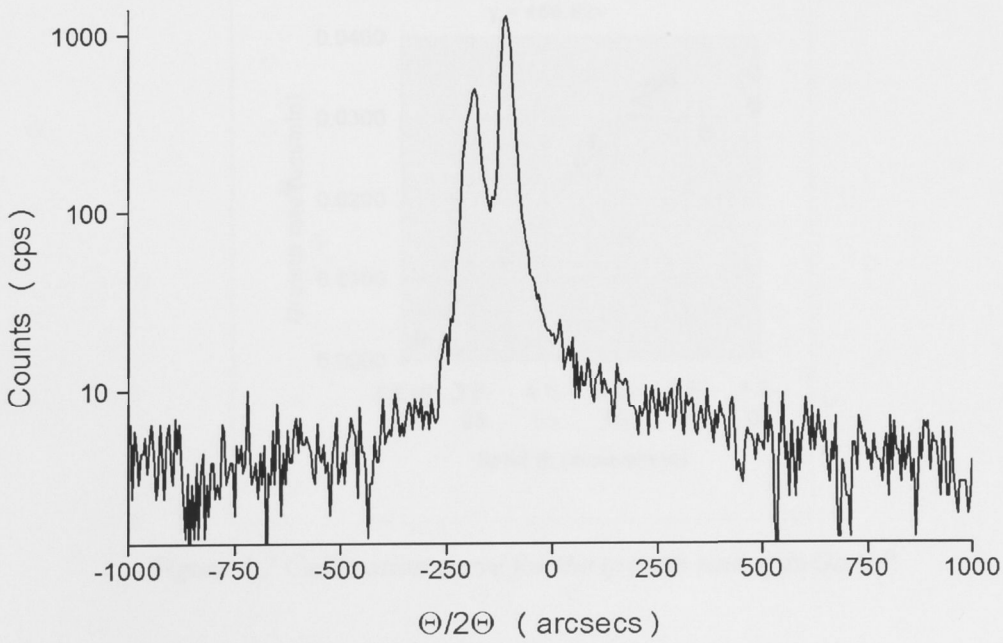

Figure 3.6 DCXRD spectrum of a 1 μm thick AlInGaAs layer grown on InP.

AlInGaAs. One of the advantages of AlInGaAs is that the lattice matching condition can be satisfied for the whole range of different Al and Ga compositions, which allows a wide range of the bandgap tuning. PL and DCXRD were used to check the composition.

Figure 3.5 illustrates the PL curve of the optimised 1 μm thick lattice-matched AlInGaAs layer designed for E_g = 1 eV. The full width at half maximum (FWHM) is only 55 nm. This is the narrowest room temperature PL ever reported for this material.

Figure 3.6 illustrates the DCXRD curve of the same sample. The main peak corresponds to the InP substrate and the secondary peak corresponds to the AlInGaAs epilayer. Although the epilayer is slightly compressively strained, a small separation between the peaks confirms a very good lattice matching of AlInGaAs layer to InP substrate.

As mentioned in chapter 2 the growth rate is controlled by the total flow of the group III precursors. Figures 3.7, 3.8 and 3.9 illustrate the growth rates for different materials used in this work. The growth rate of InGaAsP can be represented by a simple relation:

$$y = 468.82x \tag{3.9}$$

where: y is the growth rate and x is the total flow of group III precursors.

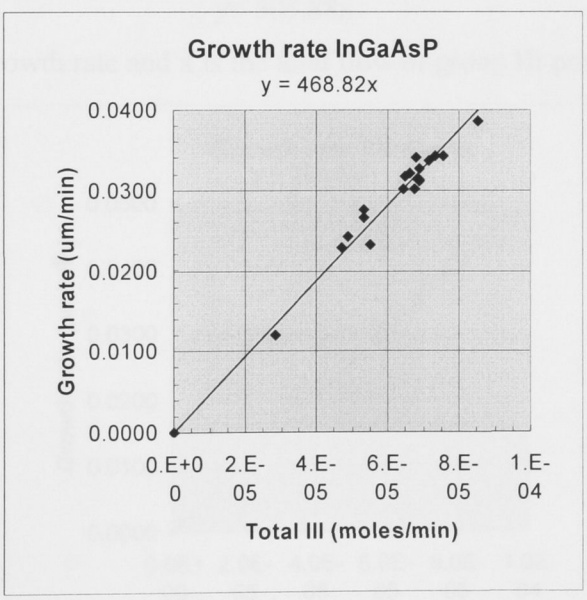

Figure 3.7 Calibration curve for the growth rate of InGaAsP.

Similarly for InGaAs the growth rate can be expressed as:

$$y = 468.73x \tag{3.10}$$

where: y is the growth rate and x is the total flow of group III precursors.

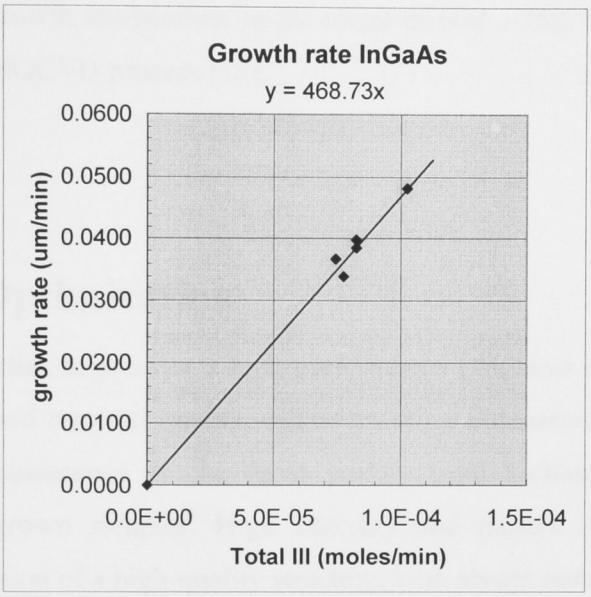

Figure 3.8 Calibration curve for the growth rate of InGaAs.

Finally for AlInGaAs the growth rate can be expressed as:

$$y = 505.88x \tag{3.11}$$

where: y is the growth rate and x is the total flow of group III precursors.

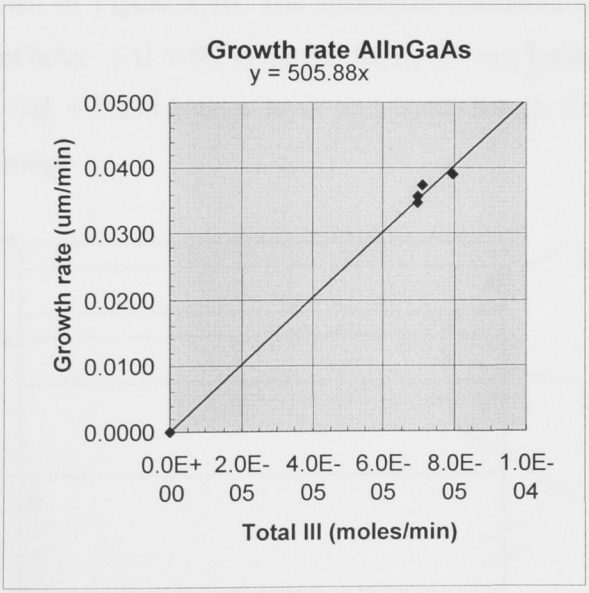

Figure 3.9 Calibration curve for the growth rate of AlInGaAs.

It is worth mentioning here that the growth rate and composition are nearly independent of the growth temperature in the range of 600 – 750 °C, which is the mass transport regime of MOCVD process [15].

3.3 Growth Optimisation

As mentioned earlier, to produce a high-performance QW laser it is essential to grow the structure with good material quality, minimum alloy fluctuation and abrupt and flat interfaces. Photoluminescence is the most widely used technique to assess these parameters of the grown samples. High intensity and narrow linewidth of the PL spectrum is an indication of a high-quality structure, with abrupt interfaces.

Alloy fluctuation and interface roughness are the main reasons for the linewidth broadening. The way to reduce alloy fluctuation, interface roughness and improve PL linewidth is to optimise growth parameters such as growth rate, growth temperature and V/III ratio of the QW layer as well as the barrier layers.

The schematic of the structures used for growth optimisation studies and AFM measurements is shown in Figure 3.10. The structures consisted of 200 nm InP buffer layer, 100 nm of AlInGaAs (Al = 0.19) barrier layer, 4.5 nm InGaAs (In = 0.65) SQW, 20 nm of AlInGaAs (Al = 0.19) barrier layer and capped with 5 nm of InP to protect AlInGaAs from oxidising.

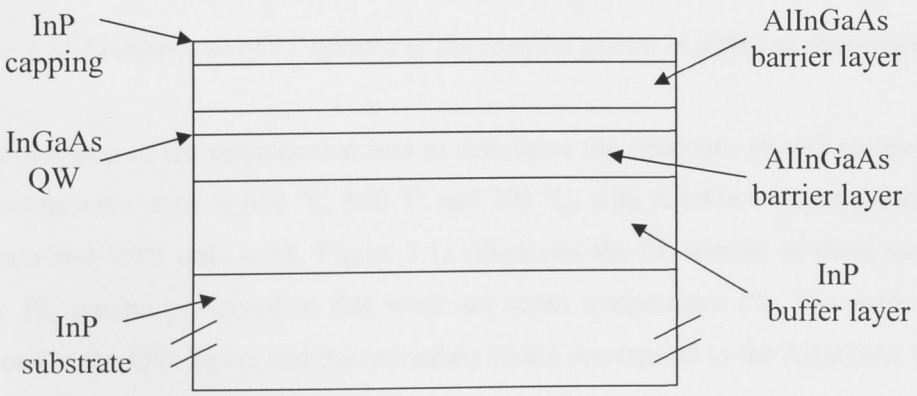

Figure 3.10 Schematic of the structures used for growth optimisation and AFM measurements.

The thick bottom AlInGaAs barrier layer allows DCXRD characterisation of the layer, while the thin top AlInGaAs barrier layer and the InP capping allow PL characterisation of the QW layer and AFM measurement of the residual roughness of the QW interfaces.

According to R. Bhat and co-authors [13] the high growth temperature and high arsine flow are necessary for growth of AlInAs with good optical and electrical properties. Later studies [4, 5, 12] report on quality improvement of the material grown at the temperature of 700 °C or higher. The reports [4, 13] also pointed out the need for high arsine flow. Although other papers [1-3, 5-12] did not specifically highlight the need for high arsine flow, they all reported the use of rather high value of V/III ratio for their growth.

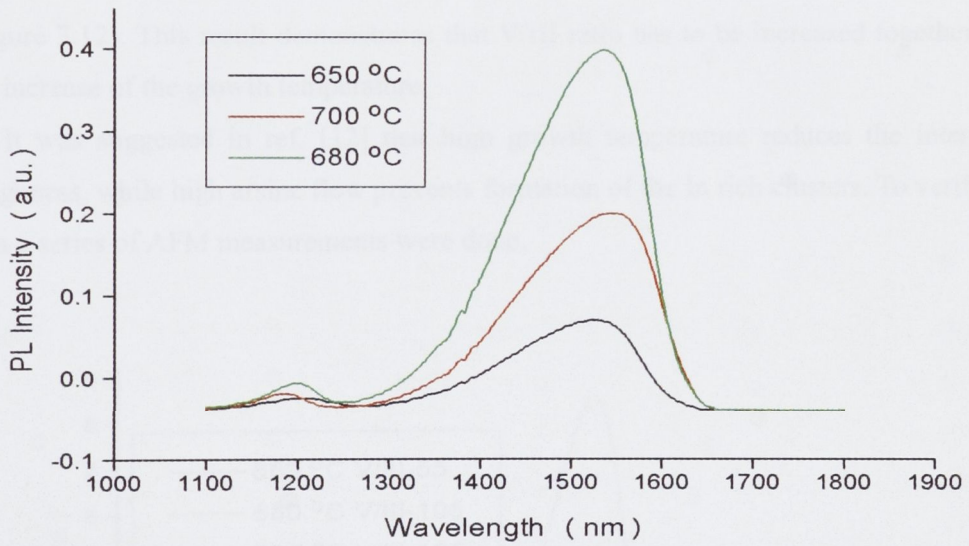

Figure 3.11 Comparison of PL spectra of the samples grown at different temperatures.

The first step of the optimisation was to determine the optimum growth temperature. The growths were done at 650 °C, 680 °C and 700 °C, with AlInGaAs layer growth rate ~2.4 μm/h and V/III ratio ~ 55. Figure 3.11 illustrates the PL spectra of these samples. (All the PL spectra presented in this work are room temperature PL. The main peaks correspond to the QW layers and the secondary peaks correspond to the AlInGaAs barrier layers).

The increase of growth temperature to 680 °C improves the PL of the sample, but

further increase of the temperature to 700 °C led to the decrease of the intensity of the PL. This was different with the results reported in ref. [1, 2, 4, 5, 6, 9, 12] where 700 °C or 720 °C growth temperature was used as an optimum growth temperature. However, other growth conditions, like V/III ratio and the growth rates also affect the quality of the material as discussed below.

As reported in the literature, high arsine flow is very important for the growth of Al containing material with good electrical and optical properties. Thus, raising V/III ratio was a logical step for improving material quality of the structure. Indeed, growing AlInGaAs at a higher V/III ratio resulted in a higher and narrower PL. Figure 3.12 illustrates these results. It is necessary to highlight that while at V/III = 55 the PL intensity of the sample grown at 700 °C was much lower than that grown at 680 °C (Figure 3.11), at V/III = 105 the sample grown at 700 °C produced much better PL (Figure 3.12). This result demonstrates that V/III ratio has to be increased together with the increase of the growth temperature.

It was suggested in ref. [12] that high growth temperature reduces the interfacial roughness, while high arsine flow prevents formation of the In rich clusters. To verify this idea a series of AFM measurements were done.

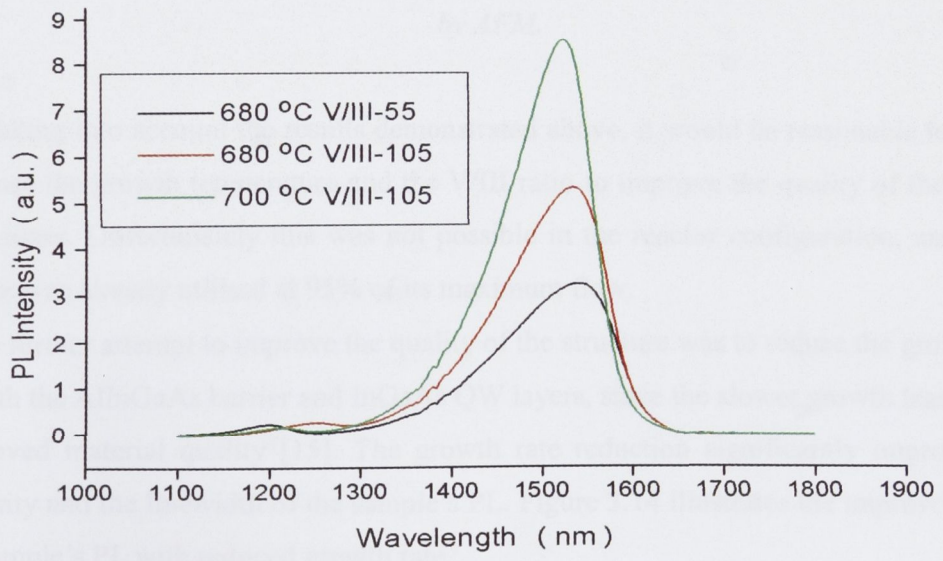

Figure 3.12 Comparison of PL spectra of the samples grown at different temperatures and V/III ratios.

The AFM results, illustrated in Figure 3.13, showed that the roughness is reduced substantially with the increase of growth temperature. This is in agreement with results reported in ref. [5, 12].

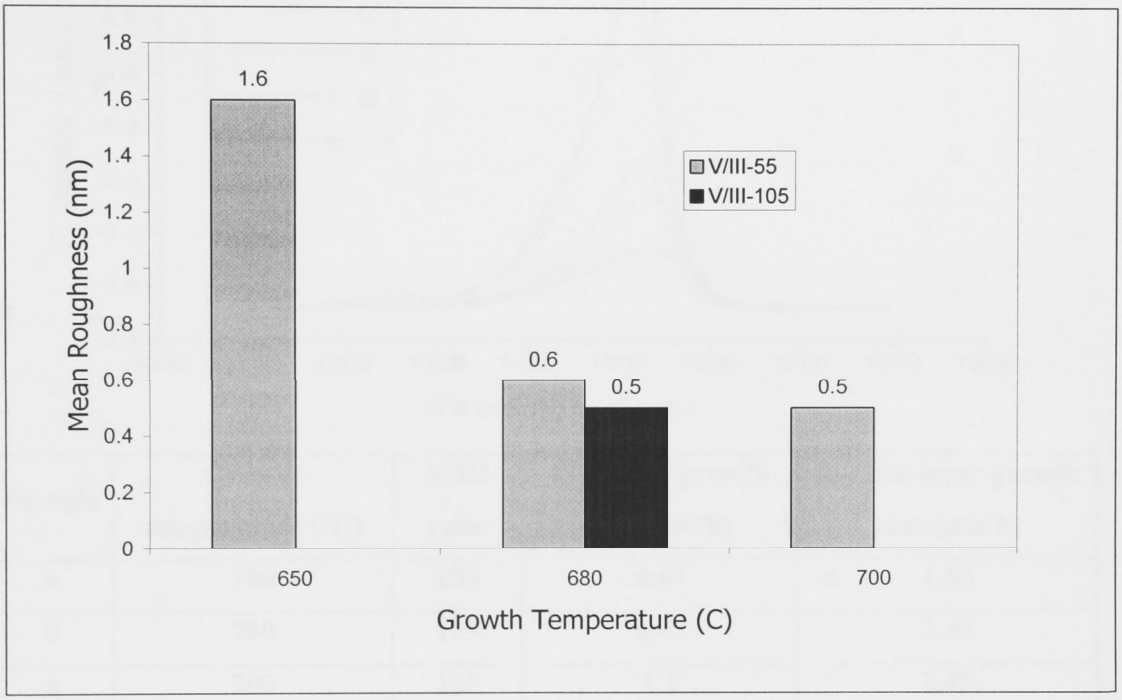

Figure 3.13 Mean roughnesses of the samples grown at different temperatures, measured by AFM.

Taking into account the results demonstrated above, it would be reasonable to further increase the growth temperature and the V/III ratio to improve the quality of the sample even more. Unfortunately this was not possible in the reactor configuration, and arsine source was already utilised at 95% of its maximum flow.

A further attempt to improve the quality of the structure was to reduce the growth rate of both the AlInGaAs barrier and InGaAs QW layers, since the slower growth leads to the improved material quality [15]. The growth rate reduction significantly improved the intensity and the linewidth of the sample's PL. Figure 3.14 illustrates the improvement of the sample's PL with reduced growth rate.

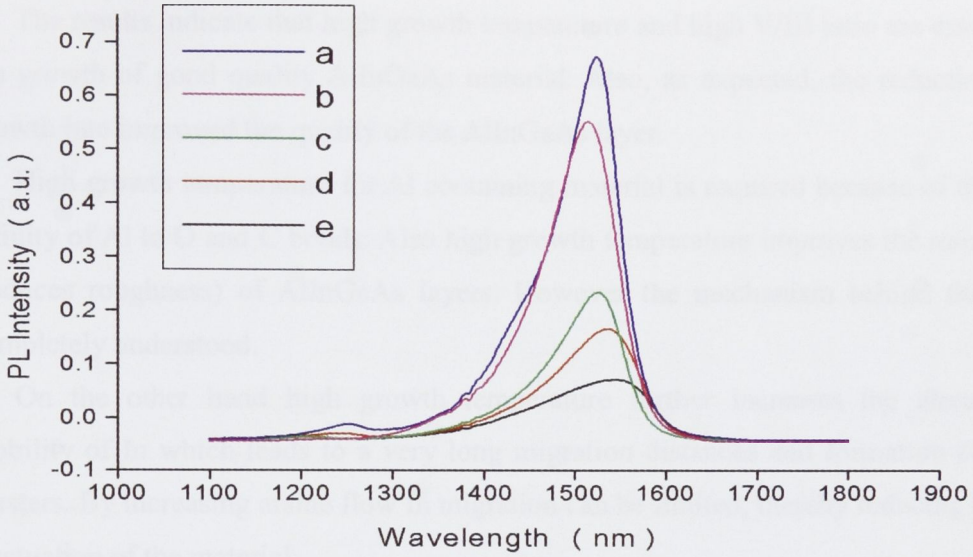

Sample	Growth temperature (^{o}C)	V/III ratio	QW layer growth rate (μm/h)	Barrier layer growth rate (μm/h)
a	700	105	0.47	1.65
b	700	105	0.47	2.45
c	700	105	1.2	2.45
d	680	105	1.2	2.45
e	680	55	1.2	2.45

Figure 3.14 Comparison of PL spectra of the samples grown at different temperature, V/III ratios and growth rates. (The table shows the details of the samples).

3.4 Conclusion

The results indicate that high growth temperature and high V/III ratio are essential for the growth of good quality AlInGaAs material. Also, as expected, the reduction of the growth rate improved the quality of the AlInGaAs layer.

High growth temperature for Al containing material is required because of the strong affinity of Al to O and C bonds. Also high growth temperature improves the morphology (reduces roughness) of AlInGaAs layers. However the mechanism behind this is not completely understood.

On the other hand high growth temperature further increases the already high mobility of In which leads to a very long migration distances and formation of In rich clusters. By increasing arsine flow In migration can be limited, thereby reducing the alloy fluctuation of the material.

The results obtained during the process of growth optimisation allow us to grow the laser structures used in Chapter 5.

References

[1] **"High-power and low-threshold-current operation of 1.3 μm strain-compensated AlGaInAs/AlGaInAs multiple-quantum-well laser diodes"**, *Po-Hsun Lei, Ming-Yuan Wu, Chia-Chien Lin, Wen-Jeng Ho, Meng-Chyi Wu, Solid-State Electronics 46 (2002), 2041-2044.*

[2] **"InGaAlAs selective-area growth on InP substrate by metalorganic vapor-phase epitaxy"**, *T. Tsuchiya, J. Shimizu, M. Shirai, M. Aoki, Journal of Crystal Growth 276 (2005), 439-445.*

[3] **"Highly selective growth of AlGaInAs assisted by CBr_4 during MOCVD growth"**, *S. Arakawa, M. Itoh, A. Kasukawa, Journal of Crystal Growth 221 (2000), 183-188.*

[4] **"Growth and characterization of InAlGaAs(P)/InGaAs(P) MQW structures"**, *W. Vanderbauwhede, X. Zhang, I. Moerman, P. Demeester, Journal of Crystal Growth 170 (1997), 738-742.*

[5] **"1.5 μm VCSEL structure optimization for high-power and high-temperature operation"**, *A. Mereuta, A. Syrbu, V. Iakovlev, A. Rudra, A. Caliman, G. suruceanu, C.-A. Berseth, E. Deichsel, E. Kapon, Journal of Crystal Growth 272 (2004), 520-525.*

[6] **"InP/InGaAlAs distributed Bragg reflectors grown by low-pressure metal organic chemical vapor deposition"**, *T.C. Lu, J.Y. Tsai, J.T. Chu, Y.S. Chang, S.C. Wang, Journal of Crystal Growth 250 (2003), 305-312.*

[7] **"Selective-area growth of high-crystalline-quality InGaAlAs by metal-organic vapor-phase epitaxy"**, *T. Tsuchiya, J. Shimizu, M. Shirai, M. Aoki, Journal of Crystal Growth 248 (2003), 384-389.*

[8] **"Phase separation in InAlAs growth by MOVPE with a low growth temperature"**, *K. Kurihara, M. Takashima, K. Sakata, R. Ueda, M. Takahara, H. Ikeda, H. Namita, T. Nakamura, K. Shimoyama, Journal of Crystal Growth 271 (2004), 341-347.*

[9] **"Design and growth of InAlAs/InGaAlAs strained-superlattice-barrier heterostructures for use in light-emitting devices",** *R.V. Chelakara, P.A. Grudowski, R.D. Dupuis, Journal of Crystal Growth 170 (1997), 595-599.*

[10] **"High-Temperature Characteristics of 1.3-μm InAsP-InAlGaAs Ridge Waveguide Lasers",** *M. Yamada, T. Anan, K. Tokutome, and S. Sugou, IEEE Photonics Technology Letters 11 (1999), 164-166.*

[11] **"MOVPE growth of AlGaInAs-InP highly tensile-strained MQWs for 1.3 μm low-threshold lasers",** *J. Decobert, N.Lagay, C. Cuisin, B. Dagens, B. Thedrez, F. Laruelle, Journal of Crystal Growth 272 (2004), 543-548.*

[12] **"Threshold Current Density Reduction of Strained AlInGaAs Quantum-Well Laser",** *J. Gilor, I. Samid, D. Fekete, IEEE Journal of Quantum Electronics 40 (2004), 1355-1364.*

[13] "Growth of high quality AlInAs by low pressure organometallic chemical vapor deposition for high speed and optoelectronic device applications", *R. Bhat, M. A. Koza, K. Kash, S. J. Allen, W. P. Hong, S. A. Schwarz, G. K. Chang and P. Lin, Journal of Crystal Growth 108 (1990), 441-448.*

[14] "High-performance 1.3 μm AlGaInAs/InP strained quantum well lasers grown by organometallic chemical vapor deposition", *R. Bhat, C. E. Zah, M. A. Koza, B. Pathak, F. Favire, W. Lin, M. C. Wang, N. C. Andreadakis, D. M. Hwang, T. P. Lee, Z. Wang, D. Darby, D. Flanders and J. J. Hsieh, Journal of Crystal Growth 145 (1994), 858-865.*

[15] "Organometallic Vapor-Phase Epitaxy: Theory and Practice" – second edition, *G.B. Stringfellow, Academic Press, San Diego (1999).*

Chapter 4

Design of the Laser Structure

4.1 Introduction

Designing of the laser structure is the initial step in the process of the laser fabrication. Properly designed laser structure will result in the required performance of the fabricated devices.

In this chapter the mathematical model used to design the laser structures will be discussed. The model uses a transfer matrix approach to determine the optical field distribution in transverse (perpendicular to the growth plane) direction. The confinement factor of each layer of the laser structure can be obtained using this model. It also utilizes a complex refractive index, which allows the determination of the optical losses in the structure.

Special attention in the modeling process was devoted to minimising the optical losses. The designed standard thick p-clad, thin p-clad and asymmetric thin p-clad structures are presented in this chapter, together with their expected optical losses.

4.2 Modeling of the Field in Transverse Direction

The mathematical model used in this work was first presented in ref. [1]. This model was developed to determine the optical field propagation of guided modes in a waveguide. The waveguide can be a simple three layer waveguide or it may consist of many layers, with complex refractive indices. The imaginary part of the refractive index of each layer describes the gain and/or losses in this layer. The electrical field in layer (i) is determined by:

$$E_i(x)=A_i \cdot e^{\beta_i(x-t_i)} + B_i \cdot e^{-\beta_i(x-t_i)} \tag{4.1}$$

where E_i is the amplitude of the electric field, A_i and B_i are the coefficients, β_i is the complex propagation constant, t_i is the position of an interface, and x is the coordinate in transverse direction. The complex propagation constant of a layer is determined by:

$$\beta_i=\frac{2\pi}{\lambda_o}\sqrt{\left(n_{ef}^2 - n_i^2\right)} \tag{4.2}$$

and the complex refractive index by:

$$n_i=n_{i\,re} - j\left(\frac{\alpha_i}{\frac{4\pi}{\lambda_o}}\right) \tag{4.3}$$

where n_{ef} is the effective refractive index, λ_o is the wavelength in free space, $n_{i\,re}$ is the real part of the refractive index of the layer, j is the imaginary unit and α_i is the absorption coefficient in the layer. The modal loss can be determined by:

$$\alpha_{\mathrm{mod}} = \frac{4\pi}{\lambda_o} n_{ef\,im} \tag{4.4}$$

where $n_{ef\,im}$ is the imaginary part of the effective refractive index.

Due to boundary condition for TE mode the electrical field and its derivative should match at the interface.

$$E_i(t_{i+1}) = E_{i+1}(t_{i+1}) \tag{4.5}$$

$$\frac{\partial}{\partial x} E_i(t_{i+1}) = \frac{\partial}{\partial x} E_{i+1}(t_{i+1}) \tag{4.6}$$

These equations can be represented in this form:

$$A_i e^{\beta_i d_i} + B_i e^{-\beta_i d_i} = A_{i+1} + B_{i+1} \tag{4.7}$$

$$A_i \beta_i e^{\beta_i d_i} - B_i \beta_i e^{-\beta_i d_i} = A_{i+1}\beta_{i+1} - B_{i+1}\beta_{i+1} \tag{4.8}$$

where d_i is the thickness of the layer (i). The thickness of the first and the last layer is set to zero, which accounts for the substrate and the air. Simplifying these equations results in:

$$A_{i+1} = \frac{A_i}{2} e^{\beta_i d_i}\left(1 + \frac{\beta_i}{\beta_{i+1}}\right) + \frac{B_i}{2} e^{-\beta_i d_i}\left(1 - \frac{\beta_i}{\beta_{i+1}}\right) \tag{4.9}$$

$$B_{i+1} = \frac{A_i}{2} e^{\beta_i d_i}\left(1 - \frac{\beta_i}{\beta_{i+1}}\right) + \frac{B_i}{2} e^{-\beta_i d_i}\left(1 + \frac{\beta_i}{\beta_{i+1}}\right) \tag{4.10}$$

These equations can be used to determine the coefficients of the field, but it is much easier to operate with them in a matrix form.

$$\begin{bmatrix} A \\ B \end{bmatrix}_{i+1} = M_{i+1} \begin{bmatrix} A \\ B \end{bmatrix}_i \tag{4.11}$$

where M_{i+1} is the complex matrix (2×2) with the coefficients determined in (4.9) and (4.10). Following this scheme, the coefficients of the last layer can be represented by the coefficients of the first layer.

$$\begin{bmatrix} A \\ B \end{bmatrix}_n = M_{tot} \begin{bmatrix} A \\ B \end{bmatrix}_1 \tag{4.12}$$

where $M_{tot}=M_2 \times M_3 \times \ldots \times M_n$.

For guided modes in the waveguide the field in the first and the last layers should be evanescent. Therefore one of the coefficients (depending on the chosen direction of the coordinates x) in both cases must be zero.

$$\begin{bmatrix} A \\ B \end{bmatrix}_1 = \begin{bmatrix} 1 \\ 0 \end{bmatrix} a \tag{4.13}$$

and

$$\begin{bmatrix} A \\ B \end{bmatrix}_n = \begin{bmatrix} 0 \\ 1 \end{bmatrix} b \tag{4.14}$$

where a and b are the coefficients. Using these equations in (4.12) results in:

$$\begin{bmatrix} 0 \\ b \end{bmatrix}_n = M_{tot} \begin{bmatrix} a \\ 0 \end{bmatrix}_1 \tag{4.15}$$

From the resulting equation:

$$M_{tot[11]}=0 \tag{4.16}$$

the values of the effective refractive index for guided modes are determined.

4.2 Minimisation of the Losses

High power operation of a laser requires minimal optical losses. Therefore special attention in the modeling process was devoted to the minimisation of the losses. Four major loss mechanisms were considered in the design process: absorption in the top metal layer, scattering at the rough interface (semiconductor-metal) caused by alloying, losses due to resonance in the contact layer and finally the free carrier absorption in highly doped regions.

As was shown in ref. [2-4], the top metal contact can strongly affect the performance of a thin p-clad laser. Standard Ti-Pt-Au as a p-side metallisation which was studied in ref. [3], shows a significant increase of the internal loss for a thin p-clad laser due to the use of Ti. Moreover it was shown that the value of the internal loss of the device is proportional to the thickness of the deposited Ti film. The same tendency was shown for the increase of the thickness of the Pt film. The lowest internal loss was measured for the devices with non-alloyed Au contact. The mechanism of this phenomenon was studied by M. Buda and co-authors [5]. They suggested that the increase of the internal loss is caused by leakage of the optical mode into the metal layer, due to high refractive index of

Ti and Pt. As for Au its refractive index is very small leading to insignificant penetration of the field into the metal layer and hence the low loss.

Although nonalloyed Au does not increase the losses, annealing of a device with Au film as a contact would have a devastating effect on the performance of the device. During the annealing process Au diffuses into the semiconductor, with diffusion length as large as 200 nm [6], creating a very rough semiconductor-metal interface. When the optical field interacts with such an interface part of it will be scattered resulting in additional optical losses. This issue was also very extensively studied in ref. [5], with the results showing that the mean roughness of 30 nm can introduce additional losses as high as 5 cm^{-1} for thin p-clad lasers.

Despite the fact that there have been some concerns about the adhesion and the resistance of non-alloyed Au contacts, a number of papers [5, 7, 8] have reported the use of non-alloyed Au contacts, with no noticeable increase of the resistance and the adhesion was good enough for most applications. These results make the use of non-alloyed Au contact a very attractive solution to the problem of the losses due to absorption in the top metal layer and scattering at the rough interface. Therefore non-alloyed Au contact was used as p-side contact for the devices fabricated in this work.

Another source of additional losses in a laser diode is the loss due to resonance in the contact layer. Normally a waveguide consists of the central region with high refractive index sandwiched between two cladding regions with lower refractive index, hence the light propagates inside the central region. In general an InP-based laser diode is a waveguide with an active region of a high refractive index and lower refractive index InP cladding layers. However it is very difficult to make a good p-side ohmic contact on InP, therefore a highly p-doped (p^{++}) InGaAs contact layer is grown on top of InP. The refractive index of the p^{++} InGaAs contact layer is much higher than the refractive index of the cladding layer, therefore a secondary waveguide is created in the structure. Due to strong coupling between the main and the secondary waveguide in a thin p-clad structure a substantial amount of the field can leak into the secondary waveguide. A high amount of the field in the highly doped region would significantly increase the modal losses. Fortunately, as was shown in ref. [9], the waveguiding effect in the secondary waveguide

occurs only at certain thicknesses of the p^{++} contact layer. The thickness of the contact layer at which this phenomenon occurs is given by:

$$d = \frac{1}{4} \cdot \frac{\lambda_o}{\sqrt{\left(n_{contact}^2 - n_{eff}^2\right)}} \tag{4.17}$$

where d is the thickness of the contact layer, λ_o is the wavelength in the free space, $n_{contact}$ is the refractive index of the contact layer and n_{eff} is the effective refractive index of the mode. This loss mechanism has to be considered during the design process of the thin p-clad laser to avoid additional modal losses.

Finally free carrier absorption in highly doped regions produces additional internal losses in thin p-clad lasers due to absorption of the field in p-doped region. This loss mechanism cannot be eliminated completely, since doping of certain regions of the laser is required for its normal operation, but it can be minimised. The internal absorption coefficient of p-doped layers is more than twice that of n-doped layers [10]. Thus this is especially important issue in the case of thin p-clad structure where highly p-doped region is very close to the active region. By introducing a trapping layer (a layer with high refractive index) into the n-doped region of the structure, a large part of the optical field is shifted into the trapping layer, and the optical field becomes asymmetric to the active region. This asymmetric design reduces the amount of the field penetrating into highly p-doped regions, hence substantially reducing the modal losses [11, 12].

4.3 The Designed Structures

In this section the designed structures will be presented, discussed and compared. Three structures were developed: standard symmetric thick p-clad structure, symmetric thin p-clad structure and asymmetric thin p-clad structure.

	λ(μm)	doping(cm^{-3})	L(nm)
$In_{0.53}Ga_{0.47}As$ (contact layer)	1.670	$p=1\cdot10^{19}$	100
InP (p-cladding)	0.922	$p=5\cdot10^{17}$	1500
InP (p-cladding)	0.922	$p=5\cdot10^{16}$	400
$In_{0.93}Ga_{0.07}As_{0.15}P_{0.85}$ (etch stop)	1.000	$p=5\cdot10^{16}$	10
InP (p-cladding)	0.922	$p=5\cdot10^{16}$	100
$In_{0.93}Ga_{0.07}As_{0.15}P_{0.85}$ (step-GRINSCH)	1.000	undoped	20
$In_{0.86}Ga_{0.14}As_{0.31}P_{0.69}$ (step-GRINSCH)	1.100	undoped	20
$Al_{0.17}Ga_{0.30}In_{0.53}As$ (barrier layer)	1.260	undoped	20
$In_{0.65}Ga_{0.35}As$ (QW)	2.005	undoped	4.8
$Al_{0.17}Ga_{0.30}In_{0.53}As$ (barrier layer)	1.260	undoped	10
$In_{0.65}Ga_{0.35}As$ (QW)	2.005	undoped	4.8
$Al_{0.17}Ga_{0.30}In_{0.53}As$ (barrier layer)	1.260	undoped	10
$In_{0.65}Ga_{0.35}As$ (QW)	2.005	undoped	4.8
$Al_{0.17}Ga_{0.30}In_{0.53}As$ (barrier layer)	1.260	undoped	10
$In_{0.65}Ga_{0.35}As$ (QW)	2.005	undoped	4.8
$Al_{0.17}Ga_{0.30}In_{0.53}As$ (barrier layer)	1.260	undoped	10
$In_{0.65}Ga_{0.35}As$ (QW)	2.005	undoped	4.8
$Al_{0.17}Ga_{0.30}In_{0.53}As$ (barrier layer)	1.260	undoped	20
$In_{0.86}Ga_{0.14}As_{0.31}P_{0.69}$ (step-GRINSCH)	1.100	undoped	20
$In_{0.93}Ga_{0.07}As_{0.15}P_{0.85}$ (step-GRINSCH)	1.000	undoped	20
InP (n-cladding)	0.922	$n=1\cdot10^{18}$	200
InP (substrate)	0.922	$n=1\cdot10^{18}$	-

Table 4.1 The symmetric thick p-clad structure. The calculated modal loss is 4.5 cm^{-1}.

The symmetric thick p-clad structure is presented in Table 4.1. The table presents the sequence of the layers, with the material composition in the first column, the value of the bandgap (expressed in wavelength) in the second column, the doping level in the third column and the thickness of the layer in the fourth column. For proper comparison of the

	λ(μm)	doping(cm^{-3})	L(nm)
$In_{0.53}Ga_{0.47}As$ (contact layer)	1.670	$p=1\cdot10^{19}$	100
InP (p-cladding)	0.922	$p=5\cdot10^{17}$	375
InP (p-cladding)	0.922	$p=5\cdot10^{16}$	25
$In_{0.93}Ga_{0.07}As_{0.15}P_{0.85}$ (etch stop)	1.000	$p=5\cdot10^{16}$	10
InP (p-cladding)	0.922	$p=5\cdot10^{16}$	100
$In_{0.93}Ga_{0.07}As_{0.15}P_{0.85}$ (step-GRINSCH)	1.000	undoped	20
$In_{0.86}Ga_{0.14}As_{0.31}P_{0.69}$ (step-GRINSCH)	1.100	undoped	20
$Al_{0.17}Ga_{0.30}In_{0.53}As$ (barrier layer)	1.260	undoped	20
$In_{0.65}Ga_{0.35}As$ (QW)	2.005	undoped	4.8
$Al_{0.17}Ga_{0.30}In_{0.53}As$ (barrier layer)	1.260	undoped	10
$In_{0.65}Ga_{0.35}As$ (QW)	2.005	undoped	4.8
$Al_{0.17}Ga_{0.30}In_{0.53}As$ (barrier layer)	1.260	undoped	10
$In_{0.65}Ga_{0.35}As$ (QW)	2.005	undoped	4.8
$Al_{0.17}Ga_{0.30}In_{0.53}As$ (barrier layer)	1.260	undoped	10
$In_{0.65}Ga_{0.35}As$ (QW)	2.005	undoped	4.8
$Al_{0.17}Ga_{0.30}In_{0.53}As$ (barrier layer)	1.260	undoped	10
$In_{0.65}Ga_{0.35}As$ (QW)	2.005	undoped	4.8
$Al_{0.17}Ga_{0.30}In_{0.53}As$ (barrier layer)	1.260	undoped	20
$In_{0.86}Ga_{0.14}As_{0.31}P_{0.69}$ (step-GRINSCH)	1.100	undoped	20
$In_{0.93}Ga_{0.07}As_{0.15}P_{0.85}$ (step-GRINSCH)	1.000	undoped	20
InP (n-cladding)	0.922	$n=1\cdot10^{18}$	200
InP substrate	0.922	$n=1\cdot10^{18}$	-

Table 4.2 The symmetric thin p-clad structure. The calculated modal loss is 8.4 cm^{-1}.

different designs, the structures were designed to be as similar as possible. Therefore only the design of the standard symmetric thick p-clad structure will be explained comprehensively, while only the changes to the structure will be discussed for symmetric thin p-clad and asymmetric thin p-clad structures.

	λ(μm)	doping(cm^{-3})	L(nm)
$In_{0.53}Ga_{0.47}As$ (contact layer)	1.670	$p=1\cdot10^{19}$	100
InP (p-cladding)	0.922	$p=5\cdot10^{17}$	375
InP (p-cladding)	0.922	$p=5\cdot10^{16}$	25
$In_{0.93}Ga_{0.07}As_{0.15}P_{0.85}$ (etch stop)	1.000	$p=5\cdot10^{16}$	10
InP (p-cladding)	0.922	$p=5\cdot10^{16}$	100
$In_{0.93}Ga_{0.07}As_{0.15}P_{0.85}$ (step-GRINSCH)	1.000	undoped	20
$In_{0.86}Ga_{0.14}As_{0.31}P_{0.69}$ (step-GRINSCH)	1.100	undoped	20
$Al_{0.17}Ga_{0.30}In_{0.53}As$ (barrier layer)	1.260	undoped	20
$In_{0.65}Ga_{0.35}As$ (QW)	2.005	undoped	4.8
$Al_{0.17}Ga_{0.30}In_{0.53}As$ (barrier layer)	1.260	undoped	10
$In_{0.65}Ga_{0.35}As$ (QW)	2.005	undoped	4.8
$Al_{0.17}Ga_{0.30}In_{0.53}As$ (barrier layer)	1.260	undoped	10
$In_{0.65}Ga_{0.35}As$ (QW)	2.005	undoped	4.8
$Al_{0.17}Ga_{0.30}In_{0.53}As$ (barrier layer)	1.260	undoped	10
$In_{0.65}Ga_{0.35}As$ (QW)	2.005	undoped	4.8
$Al_{0.17}Ga_{0.30}In_{0.53}As$ (barrier layer)	1.260	undoped	10
$In_{0.65}Ga_{0.35}As$ (QW)	2.005	undoped	4.8
$Al_{0.17}Ga_{0.30}In_{0.53}As$ (barrier layer)	1.260	undoped	20
$In_{0.86}Ga_{0.14}As_{0.31}P_{0.69}$ (step-GRINSCH)	1.100	undoped	20
$In_{0.93}Ga_{0.07}As_{0.15}P_{0.85}$ (step-GRINSCH)	1.000	undoped	350
$In_{0.79}Ga_{0.21}As_{0.45}P_{0.55}$ (trapping layer)	1.200	undoped	190
InP (n-cladding)	0.922	$n=1\cdot10^{18}$	200
InP substrate	0.922	$n=1\cdot10^{18}$	-

Table 4.3 The asymmetric thin p-clad structure. The calculated modal loss is 3.5 cm^{-1}.

As was mentioned earlier, at certain thickness of the contact layer a resonance can occur resulting in the creation of a secondary waveguide. Hence to avoid this effect the thickness of the contact layer is set to 100 nm. A good quality p-side ohmic contact

requires a highly doped contact layer especially in the case of non-alloyed contact, thus the InGaAs layer is highly doped ($p = 10^{19}$ cm^{-3}).

The thick (2 μm) InP cladding is divided into two regions with different doping concentrations, this is done to reduce the optical losses while maintaining a low series resistance of the device. A thin (10 nm) InGaAsP etch-stop layer is placed inside the second region of the cladding.

The cladding layer is followed by the standard step-graded index separate confinement heterostructure (step-GRINSCH), consisting of 20 nm of lattice matched InGaAsP ($\lambda = 1$ μm) and 20 nm of lattice matched InGaAsP ($\lambda = 1.1$ μm).

The active region consists of five compressively strained 4.8 nm thick InGaAs quantum wells (QW), separated by lattice matched AlInGaAs ($\lambda = 1.26$ μm) barriers. The number of QWs is a compromise between high gain and good material quality, since higher number of strained QWs could potentially lead to defects due to strain accumulation.

Finally a symmetrical step-GRINSCH region is placed in the n-side of the structure. The structures are grown on n-doped InP substrates ($n = 10^{18}$ cm^{-3}), with 200 nm InP n-cladding (buffer) layer.

The refractive index profile and the optical field profile of the symmetric thick p-clad structure are illustrated in Figure 4.1. This figure illustrates that the maximum of the optical field is located in the active region of the structure and the field is symmetric to the active region. The field penetration into the highly p-doped contact layer is negligible.

The calculated modal loss for this structure is 4.5 cm^{-1} which would be a reasonably good value for InP-based lasers.

The symmetric thin p-clad structure is shown in Table 4.2. As was mentioned earlier minimal changes were introduced in the structure to make direct comparison of the structures. The total thickness of the InP p-cladding layer of this structure is reduced to 500 nm, while it is still divided into two regions with the same doping level as in the symmetric thick p-clad structure. Its refractive index profile and the optical field profile are illustrated in Figure 4.2. While the maximum of the optical field is still in the active

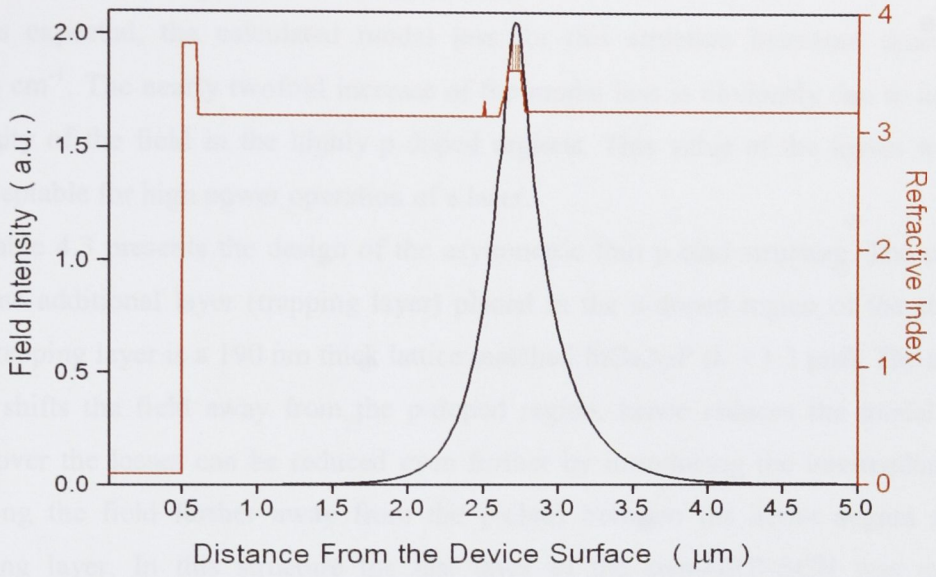

Figure 4.1 Refractive index profile and optical field distribution in the symmetric thick p-clad structure, with non-alloyed Au contact.

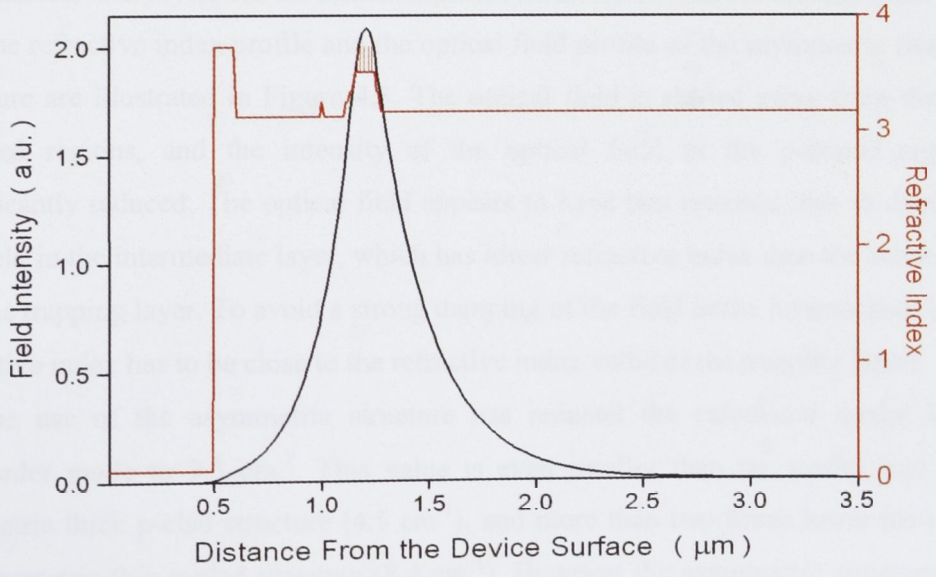

Figure 4.2 Refractive index profile and optical field distribution in the symmetric thin p-clad structure, with non-alloyed Au contact.

region, the intensity of the field in the highly p-doped regions is substantially higher than in the case of the symmetric thick p-clad structure.

As expected, the calculated modal loss for this structure increased dramatically to 8.4 cm^{-1}. The nearly twofold increase of the modal loss is obviously due to increased intensity of the field in the highly p-doped regions. This value of the losses would be unacceptable for high power operation of a laser.

Table 4.3 presents the design of the asymmetric thin p-clad structure. The structure has one additional layer (trapping layer) placed in the n-doped region of the structure. The trapping layer is a 190 nm thick lattice matched InGaAsP (λ = 1.2 μm). The trapping layer shifts the field away from the p-doped region, hence reduces the modal losses. Moreover the losses can be reduced even further by introducing the intermediate layer (shifting the field further away from the p-clad) between the active region and the trapping layer. In this structure the last layer of the step-GRINSCH was extended to 350 nm. It has to be mentioned that the thickness of the trapping layer and the intermediate layer cannot be increased indefinitely, since higher order modes start to dominate. The single mode operation can only be guaranteed if the confinement factor in the quantum well layers for the fundamental mode is higher than for the first order mode.

The refractive index profile and the optical field profile of the asymmetric thin p-clad structure are illustrated in Figure 4.3. The optical field is shifted away from the highly p-doped regions, and the intensity of the optical field in the p-doped regions is significantly reduced. The optical field appears to have two maxima, due to damping of the field in the intermediate layer, which has lower refractive index than the active region and the trapping layer. To avoid a strong damping of the field in the intermediate layer its refractive index has to be close to the refractive index value of the trapping layer.

The use of the asymmetric structure has reduced the calculated modal loss for zero-order mode to 3.5 cm^{-1}. This value is even smaller than the modal loss for the symmetric thick p-clad structure (4.5 cm^{-1}), and more than two times lower than that of the symmetric thin p-clad structure (8.4 cm^{-1}). However the asymmetric structure would require higher injection current to provide the same modal gain as in case of the symmetric structure, due to lower confinement factor in the active region.

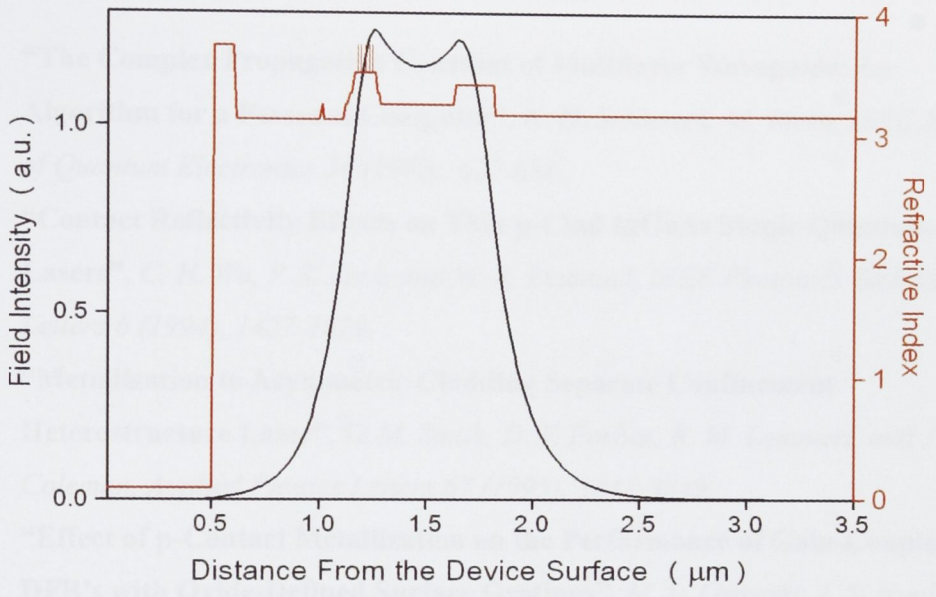

Figure 4.3 Refractive index profile and optical field distribution in the asymmetric thin p-clad structure, with non-alloyed Au contact.

These results show a clear potential for the use of asymmetric design in high power single mode InP-based lasers.

References

[1] **"The Complex Propagation Constant of Multilayer Waveguide: An Algorithm for a Personal Computer"**, *K. H. Schlereth, M. Tacke, IEEE Journal of Quantum Electronics 26 (1990), 627-630.*

[2] **"Contact Reflectivity Effects on Thin p-Clad InGaAs Single Quantum-Well Lasers"**, *C. H. Wu, P. S. Zory, and M. A. Emanuel, IEEE Photonics Technology Letters 6 (1994), 1427-1429.*

[3] **"Metallization to Asymmetric Cladding Separate Confinement Heterostructure Laser"**, *G. M. Smith, D. V. Forbes, R. M. Lammert, and J. J. Coleman, Applied Physics Letters 67 (1995), 3847-3849.*

[4] **"Effect of p-Contact Metallization on the Performance of Gain-Coupled DFB's with Oxide-Defined Surface Gratings"**, *M. L. Osowski, J. S. Hughes, and J. J. Coleman, IEEE Photonics Technology Letters 10 (1998), 926-928.*

[5] **"Low Loss, Thin p-clad 980-nm InGaAs Semiconductor Laser Diodes With an Asymmetric Structure Design"**, *M. Buda, J. Hay, H.H. Tan, J. Wong-Leung, and C. Jagadish, IEEE Journal of Quantum Electronics 39 (2003), 625-633.*

[6] **"Scanning transmission electron microscopy study of Au/Zn/Au/Cr/Au and Au/Ti/Au/Cr/Au contacts to p-type InGaAs/InP"**, *J.S. Huang, C.B. Vartuli, Journal of Applied Physics 93 (2003), 5196-5200.*

[7] **"Characteristics of MOCVD-Grown Thin p-Clad InGaAs Quantum-Dot Lasers"**, *P. Lever, M. Buda, H.H. Tan and C. Jagadish, IEEE Photonics Technology Letters 16 (2004), 2589-2591.*

[8] **"Improvement of the Kink-Free Operation in Ridge-Waveguide Laser Diodes Due to Coupling of the Optical Field to the Metal Layers Outside the Ridge"**, *M. Buda, H.H. Tan, L. Fu, L. Josyula, and C. Jagadish, IEEE Photonics Technology Letters 15 (2003), 1686-1688.*

[9] **"Low-Confinement High-Power Semiconductor Lasers"**, *M. Buda, PhD Dissertation, Technical University of Eindhoven 1999.*

[10] **"Handbook of Semiconductor Lasers and Photonic Integrated Circuits",** *edited by Y. Suematsu and A.R. Adams, Chapman & Hall, London, UK (1994).*

[11] **"High Power CW Output from Low Confinement Asymmetric Structure Diode Laser",** *G. Jordache, M. Buda, G.A. Acket, T.G. van de Roer, L.M.F. Kaufmann, F. Karouta, C. Jagadish and H.H. Tan, Electronics Letters 35 (1999), 148-149.*

[12] **"Low-Loss Low-Confinement GaAs-AlGaAs DQW Laser Diode with Optical Trap Layer for High-Power Operation",** *M. Buda, W.C. van der Vleuten, Gh. Iordache, G.A. Acket, T.G. van de Roer, C.M. van Es, B.H. van Roy, and E. Smalbrugge, IEEE Photonics Technology Letters 11 (1999), 161-163.*

Chapter 5

Characterisation of Lasers

5.1 Introduction

The characterisation of the devices is a very important step in the design and fabrication process of the lasers. Quantitative interpretation of the laser performance not only provides insights into the fundamental processes occurring in the devices, but also allows for further improvement of the devices.

In this chapter the characterisation results of the devices will be presented and analysed. The first part of this chapter will be devoted to the standard thick p-clad lasers. The characteristics of these lasers are evaluated and compared with those reported in the literature for the lasers with similar design. In the second part, characteristics of the thin p-clad lasers will be compared with those of the thick p-clad lasers. And in the conclusion the results will be discussed, and the ways to improve the performance of the devices will be outlined.

5.2 Thick p-Clad Lasers

Both sets of devices thin and thick p-clad were tested under the same conditions. The lasers were mounted on the testing stage p-side up and driven by the pulsed injection current with pulse length 2 μs and duty cycle of 5 %. The injection current ranged from 0 to 500 mA. The facets were as-cleaved, without any high reflective or anti reflective coatings. To determine characteristic temperature of the device, a series of light-current (L-I) curves were measured at different temperature (10, 20, 30, 40, 50 °C). Spectral characteristics were measured by coupling the laser light into a single mode optical fiber connected to optical spectrum analyser.

Figure 5.1 illustrates the typical L-I curve of the thick p-clad lasers, measured at 10 °C, the length of the devices was 0.5mm. Lasers with these cavity lengths have a typical threshold current of ~ 80 mA. Due to the limitation of the maximum output current of the laser diode driver, broad-area lasers (~ 50 μm) could not be tested. Hence, the threshold current density was calculated using the results obtained from 4 μm ridge devices.

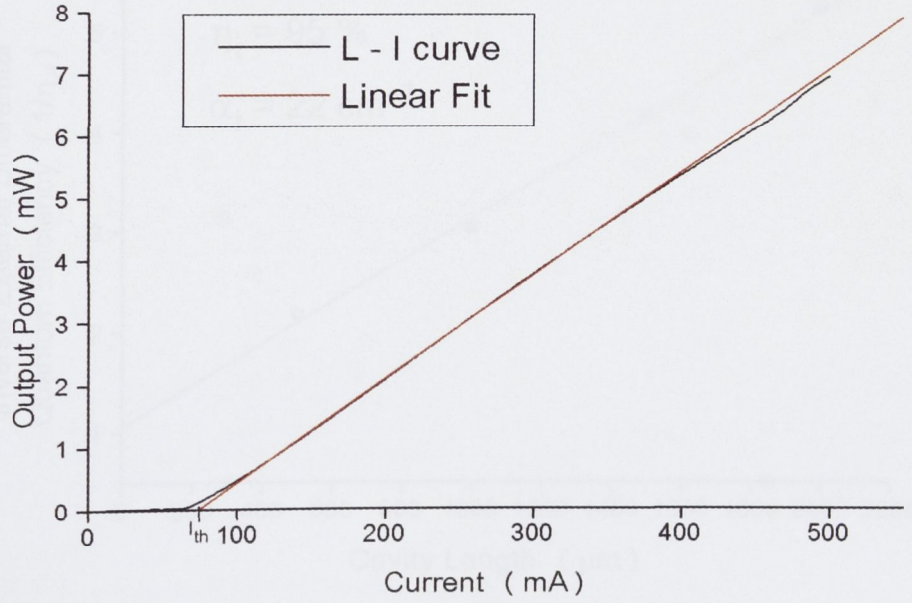

Figure 5.1 L-I curve of one of the thick p-clad lasers. The device length is 0.5 mm, duty cycle of the injection current is 5 %.

Although these were nominally 4 μm ridge lasers, from the SEM image of the laser (not shown here) the width of the bottom of the ridge was determined to be 11.6 μm. Using this value of the ridge width to determine the threshold current density resulted in the value of 1397 A/cm^2. Taking into account that there is still some current spreading under the ridge, this value is slightly higher than those reported in the literature (1000 – 1100 A/cm^2) for similar devices [7, 13].

The dependence of the inverse external differential quantum efficiency from the cavity length of the lasers is shown in Figure 5.2. From this graph a very high value of the internal quantum efficiency of 95 % was determined. This value of the internal quantum efficiency is an indication of the very good material quality of the structure. To the best of our knowledge there has been only one report [4] of the internal quantum efficiency higher than 90 % for the similar devices.

The internal losses of these lasers were determined to be 22 cm^{-1}, which is much higher than predicted by the modeling 4.5 cm^{-1}.

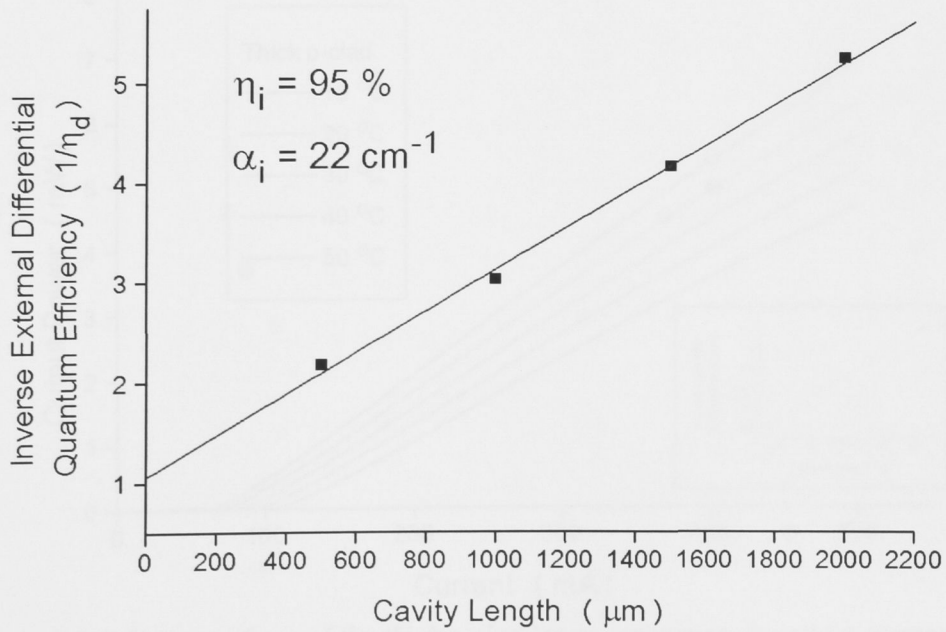

Figure 5.2 The dependence of the inverse external differential quantum efficiency of the thick p-clad lasers from the cavity length of those lasers. The squares represent the average of the measured data and the solid line is the linear fit.

The values of α_i reported in the literature for the similar ridge-waveguide lasers were in the range of 9 cm^{-1} – 27 cm^{-1} [1, 2, 3, 4, 9, 10]. High internal losses of the devices probably originate from the fabrication process. Although grown-in (material related) defects may absorb light, the presence of these sort of defects in the structure is unlikely since the devices have a very high value of the internal quantum efficiency. The most likely cause of these losses is the rough surface outside the ridge formed during the etching step of the fabrication process. Due to high phosphorus concentration of the etch stop layer the HCl based etching solution made the surface of the layer very rough. Therefore the optimisation of the etching process, in particular the etching depth and the material composition of the etch stop layer would decrease the value of the losses and greatly improve the performance of these lasers.

Figure 5.3 illustrates a set of the L-I curves measured at different temperatures, to determine the characteristic temperature of the laser, and the inset shows the variation of the threshold current with the increasing temperature.

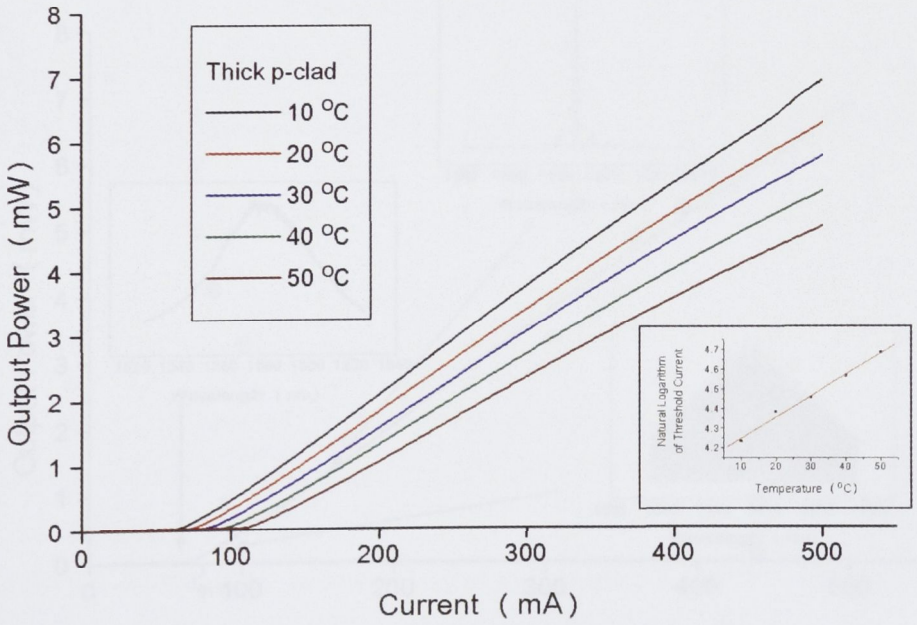

Figure 5.3 L-I curves of one of the thick p-clad lasers, operating at various temperatures. The inset shows the variation of the threshold current with the increasing temperature.

The expected improvement of the characteristic temperature is the main reason for the use of aluminum containing materials in InP based lasers. Indeed, this work, as well as all the other works done on AlInGaAs/InP material system, showed a great improvement in thermal stability of the AlInGaAs/InP based laser over conventional InGaAsP/InP based lasers. The value obtained in this work of the characteristic temperature for the thick p-clad lasers (T_0 = 85 K) was about 20 % higher than the standard values for the conventional InGaAsP/InP based lasers. This value of T_0 is very close to the results reported in the literature [1, 4, 6, 8, 10, 13] for the similar lasers with as-cleaved facets.

In figure 5.4 the spectral behaviour of the laser is shown. The insets illustrate the spectrum of the laser radiation before the threshold, just after the threshold and well above the threshold.

It is useful to know the effect of the operational temperature on the center wavelength or the lasing wavelength of the laser. Figure 5.5 illustrates the center wavelength change of the thick p-clad lasers as a function of the operation temperature.

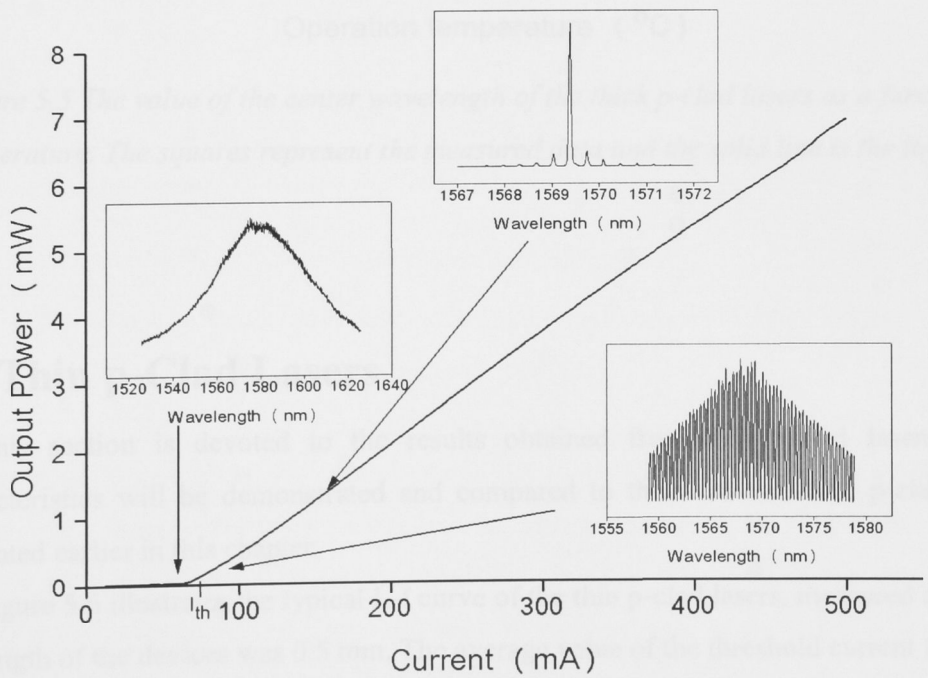

Figure 5.4 L-I curve of one of the thick p-clad lasers, with the insets illustrating the spectrum of the laser radiation at different values of the injection current.

The lasing wavelength changed from 1565 nm at 10 °C to 1587 nm at 50 °C, and slope of the linear fit was measured to be 0.55 nm/ °C.

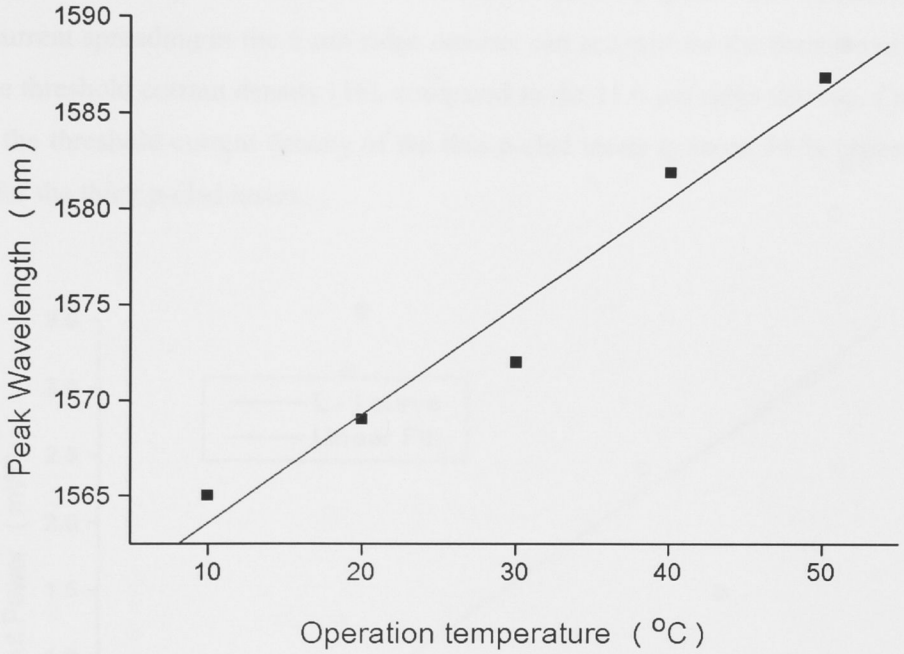

Figure 5.5 The value of the center wavelength of the thick p-clad lasers as a function of temperature. The squares represent the measured data and the solid line is the linear fit.

5.3 Thin p-Clad Lasers

This section is devoted to the results obtained from thin p-clad lasers. Their characteristics will be demonstrated and compared to those of the thick p-clad lasers presented earlier in this chapter.

Figure 5.6 illustrates the typical L-I curve of the thin p-clad lasers, measured at 10 °C, the length of the devices was 0.5 mm. The average value of the threshold current for these lasers was 82 mA. This is almost the same value as for the thick p-clad lasers (81 mA). This was unexpected, as thin p-clad lasers are predicted to have higher losses and as a result higher threshold current than thick p-clad devices.

Due to the nature of the wet etching process the bottom of the ridge of the thin p-clad lasers is much narrower (6 μm) than that of the thick p-clad lasers (11.6 μm), even though the nominal ridge was supposed to be 4 μm wide. Using this value the threshold current density of the thin p-clad lasers was calculated to be 2733 A/cm^2. The increased effect of the current spreading in the 6 μm ridge devices can account for the increase of 1.5 times of the threshold current density [16], compared to the 11.6 μm ridge devices. Considering this, the threshold current density of the thin p-clad lasers is about 30 % higher than the one for the thick p-clad lasers.

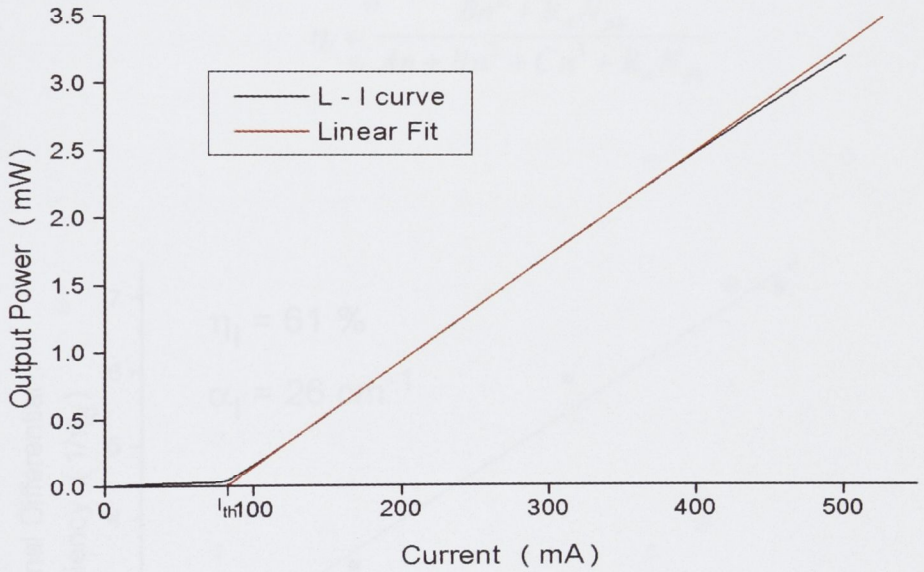

Figure 5.6 L-I curve of one of the thin p-clad lasers. The device length is 0.5 mm, duty cycle of the injection current is 5 %.

Shown in Figure 5.7 is the dependence of the inverse external differential quantum efficiency as a function of the cavity length for the thin p-clad lasers. The slope of the linear fit gives the value of 26 cm^{-1}. Though this value of internal losses is also much higher than the calculated value, the difference in losses of only 4 cm^{-1} between thin and thick p-clad structures correlates well with the prediction made during the design process. But this value of losses does not fully explain the increase of the threshold current density.

Surprisingly, the internal quantum efficiency of these lasers was only 61 %, which explains their high threshold current density. It appears surprising that the thin p-clad devices have such a low η_i compared to thick p-clad devices, even though both have very similar structures (the only difference is the thickness of the p-clad layer).

The increase in losses leads to an increase of carrier density needed for lasing, which in turn leads to higher Auger recombination, hence decreases the internal quantum efficiency.

The internal quantum efficiency is given by:

$$\eta_i = \frac{Bn^2 + R_{st}N_{ph}}{An + Bn^2 + Cn^3 + R_{st}N_{ph}} \tag{5.1}$$

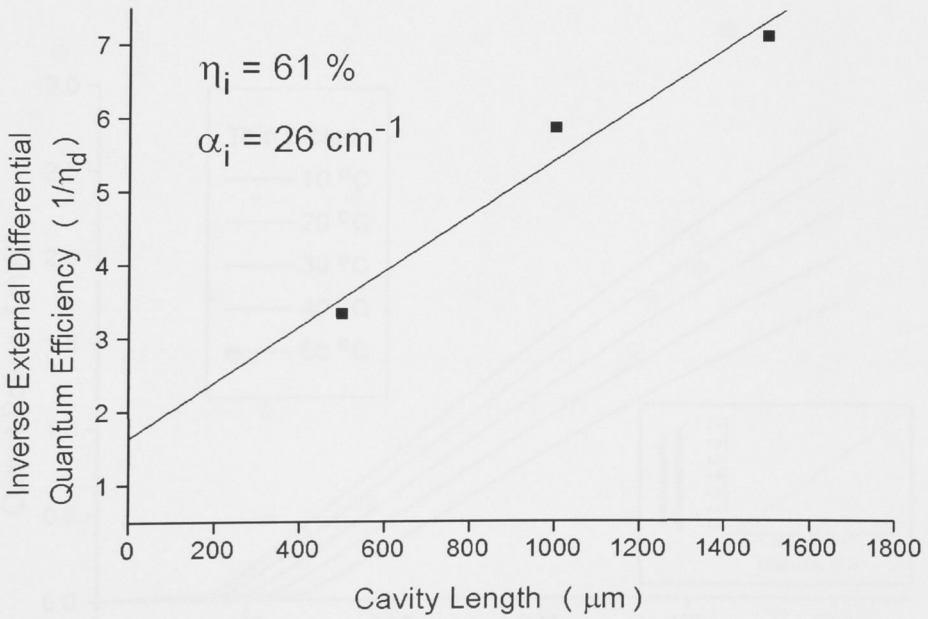

Figure 5.7 The dependence of the inverse external differential quantum efficiency of the thin p-clad lasers from the cavity length of those lasers. The squares represent the average of the measured data and the solid line is the linear fit.

where A is the coefficient of nonradiative recombination, B the coefficient of spontaneous radiative recombination, C the coefficient of Auger recombination, R_{st} the coefficient of stimulated emission rate, N_{ph} the intracavity photon density, n the carrier density. Normally the radiative terms of this equation ($Bn^2 + R_{st}N_{ph}$) dominate the recombination process, making $\eta_i \sim 1$, but at high carrier densities Auger recombination increases rapidly, quickly overcoming the spontaneous radiative recombination [15]. The use of highly reflective facet coatings would increase the radiative stimulated recombination by increasing the intracavity photon density hence improving the value of the internal quantum efficiency.

As Auger recombination increases even more with temperature, it would certainly degrade the thermal stability of the lasers. Indeed, this was observed for the thin p-clad lasers where the characteristic temperature was measured to be only 58 K. This is a significant drop of T_0 in comparison to 85 K for thick p-clad lasers. Figure 5.8 illustrates the set of the L-I curves measured at different temperatures to determine the characteristic

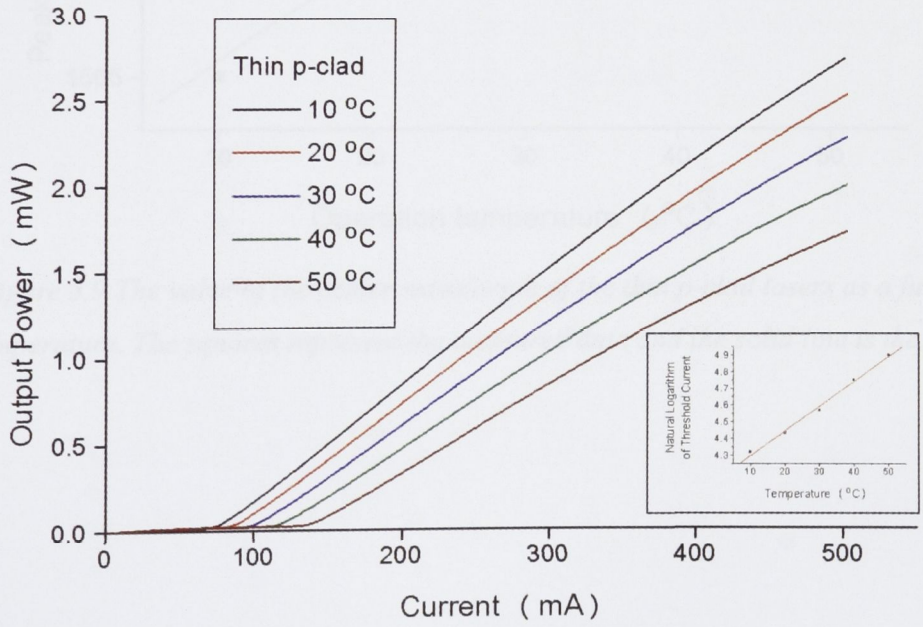

Figure 5.8 L-I curves of one of the thin p-clad lasers, operating at various temperatures. The inset shows the variation of the threshold current with the increasing temperature.

temperature of the laser and the inset shows the variation of the threshold current with the increasing temperature.

In Figure 5.9 the center wavelength change of the thin p-clad lasers as a function of the operation temperature is shown. The slope of the linear fit for thin p-clad devices is 0.5 nm/ °C, which is similar to that of the thick p-clad lasers, since they are of the similar design.

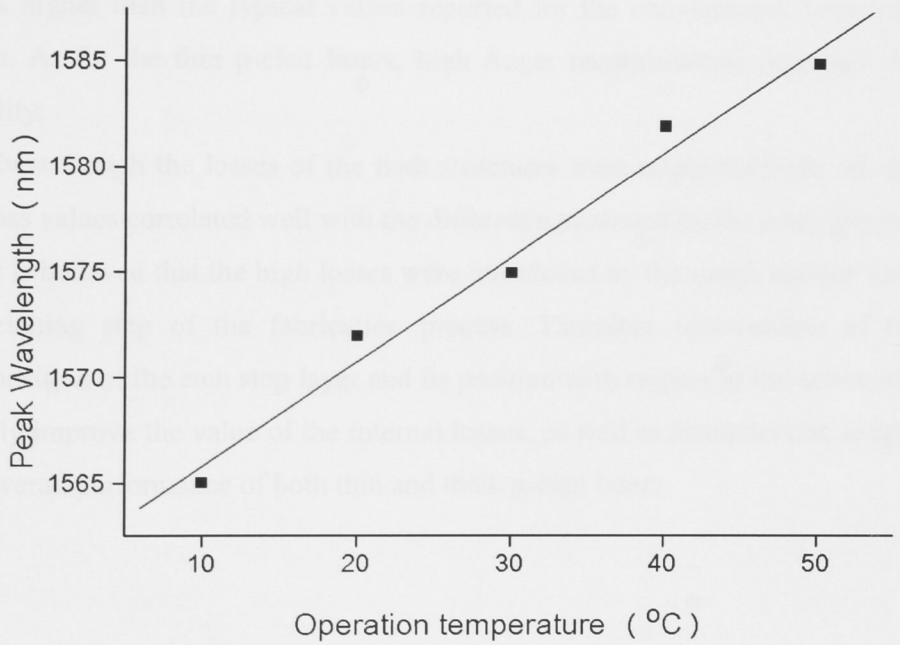

Figure 5.9 The value of the center wavelength of the thin p-clad lasers as a function of temperature. The squares represent the measured data and the solid line is the linear fit.

5.4 Conclusion

High material quality of the structures was demonstrated by the internal quantum efficiency of 95 % of the thick p-clad lasers, one of the highest ever reported for AlInGaAs/InP ridge waveguide lasers. Although the internal quantum efficiency of thin p-clad lasers was significantly lower, it was explained to be due to increased Auger recombination.

The characteristic temperature T_0, for the thick p-clad lasers was 85 K which is about 20 % higher than the typical values reported for the conventional InGaAsP/InP based lasers. As for the thin p-clad lasers, high Auger recombination degraded their thermal stability.

Even though the losses of the both structures were relatively high, the difference in the loss values correlated well with the difference predicted by the designing process.

It is believed that the high losses were introduced by the rough surface formed during the etching step of the fabrication process. Therefore optimisation of the material composition of the etch stop layer and its position with respect to the active region would greatly improve the value of the internal losses, as well as characteristic temperature and the overall performance of both thin and thick p-clad lasers.

References

[1] **"1.57 μm Strained-Layer Quantum Well GaInAlAs Ridge-Waveguide Laser Diodes with High Temperature (130°C) and Ultrahigh-Speed (17 GHz) Performance",** *B. Stegmuller, B. Borchert, and R. Gessner, IEEE Photonics Technology Letters 5 (1993), 597-599.*

[2] **"1.3-μm AlGaInAs Strain Compensated MQW-Buried-Heterostructure Laser for Uncooled 10-Gb/s Operation",** *Takahiro Nakamura, Associate Member, IEEE, Tetsuro Okuda, Ryuji Kobayashi, Yoshiharu Muroya, Kiyotaka Tsuruoka, Youichi Ohsawa, Takumi Tsukuda, and Shin Ishikawa, IEEE Journal of Selected Topics in Quantum Electronics 11 (2005), 141-148.*

[3] **"Low-Threshold and High-Temperature Operation of InGaAlAs-InP Lasers",** *T.R. Chen, P.C. Chen, J. Ungar, M.A. Newkirk, S. Oh, and N. Bar-Chain, IEEE Photonics Technology Letters 9 (1997), 17-18.*

[4] **"High-performance phosphorus-free 1.3 μm AlGaInAs/InP MQW lasers",** *Jen-Wei Pan, Ming-Hong Chen, Jen-Inn Chyi, Journal of Crystal Growth 201/202 (1999), 923-926.*

[5] **"High Temperature Characteristics of Strained InGaAs/InGaAlAs Quantum Well Lasers",** *Seoung-Hwan Park, Japanese Journal of Applied Physics 36 (1997), 3528-3530.*

[6] **"Thermal Properties of 1.3 μm AlGaInAs Multi Quantum Well Ridge Waveguide Lasers",** *M. Kubota, K. Hamano, K. Takemasa, M. Kobayashi, H. Wada, T. Munakata, Japanese Journal of Applied Physics 39 (2000), 2297-2300.*

[7] **"Design and Characterization of 1.3-μm AlGaInAs-InP Multiple-Quantum-Well Lasers",** *Sandra R. Selmic, Tso-Min Chou, JiehPing Sih, Jay B. Kirk, Art Mantie, Jarome K. Butler, David Bour and Gary A. Evans, IEEE Journal on Selected Topics in Quantum Electronics 7 (2001), 340-349.*

[8] **"Highly Uniform Characteristics 12-element 1.5 μm Strain-Compensated AlGaInAs/InP Laser Arrays with Low Threshold Current and High Characteristic Temperature",** *Chia-Chien Lin, Kuo-Shung Liu, Meng-Chyi Wu*

and Hung-Pin Shiao, Electronics Letters 34 (1998), 186-187.

[9] **"Effects of Well Number on Temperature Characteristics in 1.3-μm AlGaInAs–InP Quantum-Well Lasers",** *Hiroshi Wada, Keizo Takemasa, Tsutomu Munakata, Masao Kobayashi, and Takeshi Kamijoh, IEEE Journal of Selected Topics in Quantum Electronics 5 (1999), 420-427.*

[10] **"Temperature-Dependent Characteristics of 1.3-m AlGaInAs–InP Lasers with Multiquantum Barriers at the Guiding Layers",** *Jen-Wei Pan, Ming-Hong Chen, Jen-Inn Chyi, and Tien-Tsorng Shih, IEEE Photonics Technology Letters 10 (1998), 1700-1702.*

[11] **"Very Low Threshold Current Density 1.5 pm GalnAs/AIGalnAs Graded-Index Separate-Confinement-Heterostructure Strained Quantum Well Laser Diodes Grown by Organometallic Chemical Vapor Deposition",** *A. Kasukawa, R. Bhat, C. E. Zah, M. A. Koza, and T. P. Lee, Applied Physics Letters 59 (1991), 2486-2488.*

[12] **"High-Power AlGalnAs Strained Multiquantum Well Lasers Operating at 1.52 μm",** *T.C. Newell, P.M. Varangis, E. Pease,* ***A.*** *Stintz, G.T. Liu, K.J. Malloy and L.F. Lester, Electronics Letters 36 (2000), 955-956.*

[13] **"Record High Characteristic Temperature (*To* = 122 K) of 1.55 μm Strain-Ccompensated AIGalnAs/AIGalnAs MQW Lasers with AIAs/AllnAs Multiquantum Barrier",** *N. Ohnoki, G. Okazaki, F. Koyama and K. Iga, Electronics Letters 35 (1999), 51-52.*

[14] **"A Theoretical Investigation of the Characteristic Temperature T_0 for Semiconductor Lasers",** *Bernd Witzigmann and Mark S. Hybertsen, IEEE Journal of Selected Topics in Quantum Electronics 9 (2003), 807-815.*

[15] **"Photoexcited Carrier Lifetime and Auger Recombination in 1.3μm InGaAsP",** *B. Sermage, H.J. Eichler, J.P. Heritage, R.J. Nelson and N.K. Dutta, Applied Physics Letters 42 (1983), 259-261.*

[16] **"The Effects of Lateral Current Spreading, Carrier outdiffusion and Optical Mode Losses on the Threshold Current Density of GaAs-AlGaAs Stripe-Geometry DH Lasers",** *W.T. Tsang, Journal of Applied Physics 49 (1978), 1031-1043.*

Chapter 6

Summary and Recommendation for Future Research

This work concentrated on the application of AlInGaAs material in InP-based lasers to improve their thermal stability and the investigation of thin p-clad design as an intermediate step to asymmetric thin p-clad structures.

The results presented in the growth section of this work showed that by increasing the V/III ratio simultaneously with the increase of the growth temperature, AlInGaAs material of a very high quality can be obtained. The optimised growth conditions allowed the growth of thick AlInGaAs layer with the PL linewidth of only 55 nm, to the best of our knowledge this is the narrowest room temperature PL spectrum ever reported for this sort of material. The growth conditions of AlInGaAs used in this work are: the growth rate – 1.65 μm/h, the growth temperature – 700 °C and the V/III ratio – 105. Although the results indicate that further increase in growth temperature and V/III ratio could further improve the material quality, this was not possible with the current design of the MOCVD reactor.

High material quality of the AlInGaAs was also demonstrated by the value of the internal quantum efficiency (95 %) of the thick p-clad lasers. This value of the internal quantum efficiency is also one of the highest ever reported for AlInGaAs lasers. Since the active regions of both structures are identical, lower internal quantum efficiency of the thin p-clad lasers of only 61 %, was explained to be due to increased Auger recombination, as a result of higher optical losses.

Characteristic temperature of the thick p-clad lasers (T_o = 85 K) was about 20 % higher than the typical values reported for the conventional InGaAsP/InP based lasers. On the other hand a high Auger recombination degraded the thermal stability of the thin p-clad lasers.

The comparison of the thick and the thin p-clad lasers showed that, although the measured values of the losses were much higher than predicted, the difference of the

optical losses of the lasers correlated well with the difference determined by the designing process. Higher than expected optical losses of the structures most likely were introduced by the rough surface formed during the etching step of the fabrication process. Therefore some optimisation of the composition of the etch-stop layer and its position with respect to the active region is required. Another option for the improvement of the etching step of the fabrication process is the use of dry etching. The low optical losses would result in lower Auger recombination and consequently higher internal quantum efficiency and better thermal stability of the devices.

The growth issue of the application of AlInGaAs in InP-based lasers has been overcome in this work. High material quality AlInGaAs was obtained and as a result the fabricated thick p-clad devices showed a very high value of internal quantum efficiency and improved thermal stability. However some optimisation of the fabrication process is required to minimise higher than expected optical losses. Subsequently high power single-mode InP-based lasers with the asymmetric thin p-clad structure can be fabricated and studied.